Modification of fumarolic gases by the ice-covered edifice of Erebus volcano, Antarctica

T. Ilanko*[1], T.P. Fischer[2], P. Kyle[3], A. Curtis[4], H. Lee[5], Y. Sano[6]

1. Department of Geography, University of Sheffield, Sheffield S10 2TN, UK

2. Department of Earth & Planetary Sciences, University of New Mexico, NM 87131, USA

3. Department of Earth & Environmental Science, N.M. Institute of Mining and Technology, Socorro, NM 87801, USA

4. Jet Propulsion Laboratory, Pasadena, CA91109, USA

5. School of Earth and Environmental Sciences, Seoul National University, 1 Gwanak-ro, Gwanak-gu, 08826 Seoul, South Korea

6. Institute of Atmosphere and Ocean Research, The University of Tokyo, Chiba, Japan

***Corresponding author: tehnuka@volcanofiles.com**

Non-peer reviewed preprint for EarthArXiv of a manuscript submitted to the Journal of Volcanology and Geothermal Research

Modification of fumarolic gases by the ice-covered edifice of Erebus volcano, Antarctica

Abstract

The chemistry of gases measured in ice caves and from warm geothermal ground at Erebus volcano, Antarctica, show that gas emissions are dominated by air, with varying amounts of added volcanic CO_2. This suggests widespread circulation of air through the volcanic edifice, as well as spatially or temporally varying contributions from magmatic degassing.

The resulting gases are further modified by two processes. The first is CO_2 dissolution in water, resulting in fractionation from magmatic $\delta^{13}C$-CO_2 values, which are estimated to be around -4‰, to heavier values, up to -1‰. Assuming all magmatic CO_2 is dissolved in neutral water as HCO_3^-, this requires hydrothermal temperatures of over 120°C. However, other phases such as calcite may be present, likely implying even higher temperatures, while lower water pH values could result in similar isotope ratios at much lower temperatures, such as 60°C at pH of 5.3. A large proportion of magmatic CO_2 must be lost to this hydrothermal system or to mixing with air. The hydrothermal influence is localized to certain areas on the volcano, which may be associated with high velocity zones identified in previous studies by seismic tomography. Two sites with stronger magmatic signatures, by contrast, are above low velocity zones representing possible shallow magma storage.

The second modification is the removal of oxygen from both deeply-sourced and air-derived gases. This is likely due to prevailing conditions in the subsurface, as it is independent of the original source of the gases and of hydrothermal modifications, and thus may affect sites with magmatic, air-like, or hydrothermal signatures.

1. Introduction

1.1 Hydrothermal systems at snow- or ice-covered volcanoes.

Near surface heat and fumarolic gas emission on glaciated and snow-covered volcanoes, cause melting and sublimation of the ice and snow and can result in the formation of fumarolic ice caves (FIC) (Curtis and Kyle, 2011, 2017). Globally, FIC have been described on only a few volcanoes, including Erebus and Mount Melbourne in Antarctica (Lyon and Giggenbach, 1974), and Mount Rainier (Zimbelman et al., 2000), Mount Baker, and Mount St Helens in the Cascades. However, it has been suggested that such systems may be more common and widely distributed than the few known examples (Curtis and Kyle, 2017).

FIC conveniently reveal fumarolic or diffuse degassing sites that might be hard to observe on a volcano without ice or snow cover. Understanding this degassing and potential hydrothermal circulation at glaciated volcanoes also has implications for volcanic hazards. These include the likelihood of phreatic or phreatomagmatic eruptions, or reduced slope stability due to hydrothermal alteration. Monitoring gas emissions or ice cover at active volcanoes could be important in identifying changes to heat flow and degassing that result from changes in shallow magmatic or hydrothermal systems. Moreover, glaciation and

deglaciation may act on a large scale as controls on volcanic activity and the climate, with the implication that decreasing ice cover can cause increases in carbon dioxide emissions, and thus warming (Huybers and Langmuir, 2009). Understanding degassing from glaciated volcanoes is important to both understanding past changes in climate and the implications of widespread ice loss in volcanic regions due to a warming climate. For example, over a hundred potential subglacial volcanoes have been identified in West Antarctica (van Wyk de Vries et al., 2018) as well as evidence for recent eruptions (Iverson et al., 2017), and possible ongoing magma movement (Lough et al., 2013).

Due to the more limited ice cover in its summit area and the accessibility of Erebus, it is one of the few sites where degassing of a glaciated volcano can be quantified. Erebus is unique among volcanoes currently hosting ice caves in that it exhibits long-term persistent degassing through an open conduit, with many studies focused on the dynamics and gas chemistry of its lava lake. However, also of interest in understanding its gas flux, and more relevant to glaciated volcanoes lacking open summit vents, is the persistent flank degassing on which our study focuses. The following section briefly describes the setting and volcanic activity of Erebus.

1.2 Tectonic setting, Antarctic volcanism and Erebus volcano

Erebus volcano (Fig 1) is one of four volcanic centres on Ross Island at the southern end of the Terror Rift, which has the youngest extension in the West Antarctic Rift System (WARS) (Hall et al., 2007; Henrys et al., 2007). Although Erebus is presently the most active volcano in the WARS, degassing occurs at others (Mt Berlin, Marie Byrd Land; Mts Rittmann and Melbourne, northern Victoria Land). The WARS covers the margin between the Transantarctic Mountains and the crustal blocks, derived from the breakup of Gondwana, that make up much of West Antarctica (Behrendt et al., 1991). Extension across the rift dates from the Cretaceous and the end of subduction along the Gondwana margin, but there remains uncertainty about whether the WARS is still active (Martin et al., 2014; Harry et al., 2018), and the relationship between its tectonism and volcanic activity.

Late Cenozoic volcanism in the WARS has been attributed to mantle plumes or extension of the lower lithosphere causing decompression melting (Kyle et al., 1992; Behrendt, 1999; Rocchi et al., 2002). According to Rilling et al. (2009), the timing of rifting episodes and volcanism in the Terror Rift indicates decompression melting, though additional heat input or a modified mantle composition with a lower solidus are required to allow partial melting and volcanism. This is consistent with Panter et al. (2018) who attribute the geochemistry of lavas in the northwest Ross Sea to subcontinental lithospheric mantle (SCLM) with metasomatic veins formed by carbonate-rich partial melt from the asthenosphere, itself containing material subducted at the Gondwana margin. Ross Island, however, may be an exception. The HIMU-like composition of Ross Island lavas, and the presence of a seismic low velocity zone down to 1200 km beneath Ross Island support the argument of Phillips et al. (2018) for upwelling from the asthenospheric mantle as the source of volcanism. A mantle plume (Kyle et al., 1992) could also account for the large volume magmatism, the radial arrangement of volcanic centres, and ongoing volcanism. No carbon isotope data are available for xenoliths on Ross Island but Correale et al. (2017) report carbon isotope ratios of -4.5‰ to -2.5‰, with -3.5‰ for samples containing high CO_2, in SCLM xenoliths from Northern Victoria Land. However, this may differ further south beneath Ross Island, given the evidence for an asthenospheric source and the suggestion by Phillips et al. (2018) that the metasomatized SCLM beneath Ross Island has been removed by mantle upwelling.

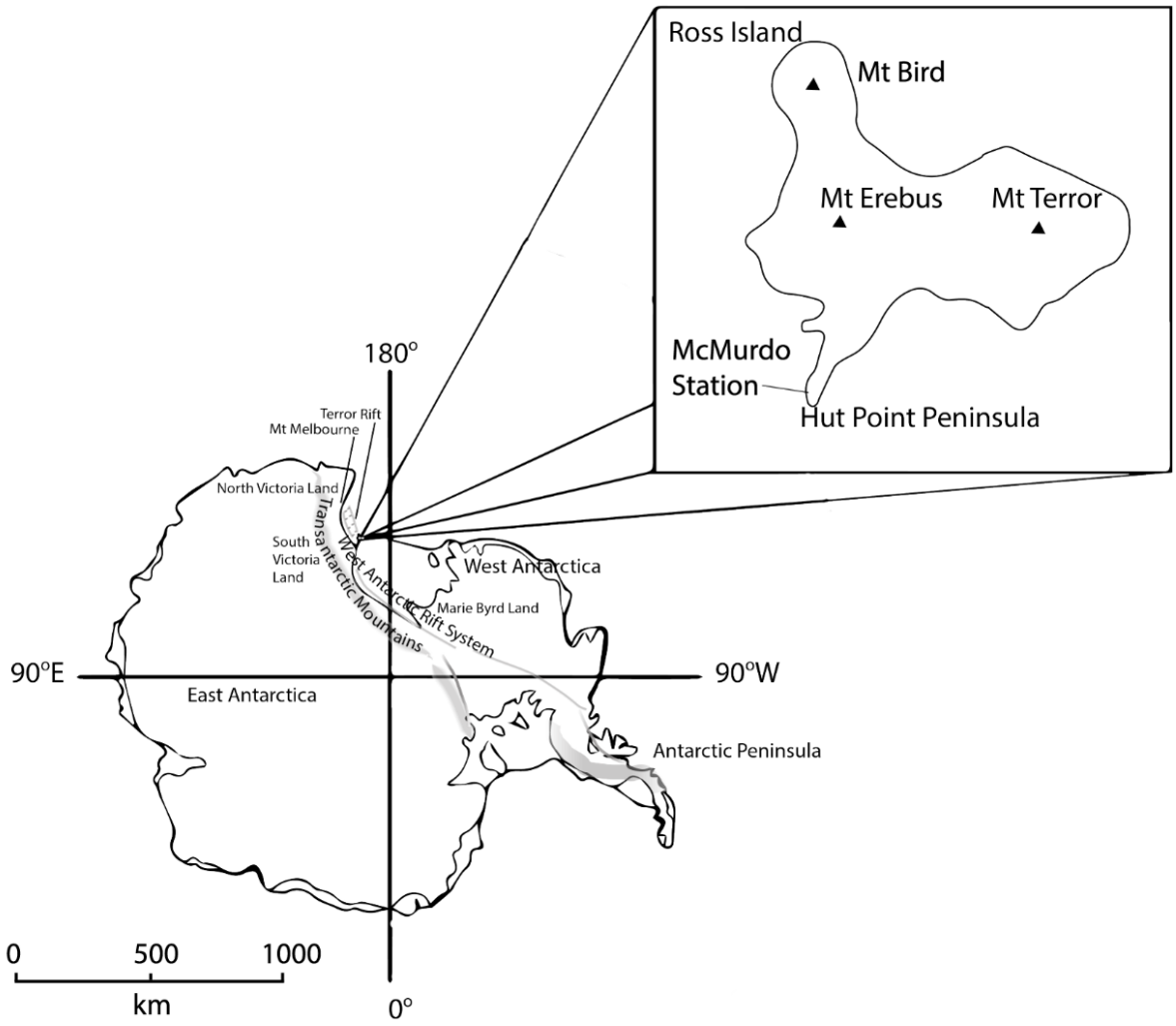

Figure 1. Location of Ross Island and Erebus. McMurdo Station and Scott Base are located on the southern end of Hut Point Peninsula. WARS and Terror Rift after LeMasurier (1990, 2008).

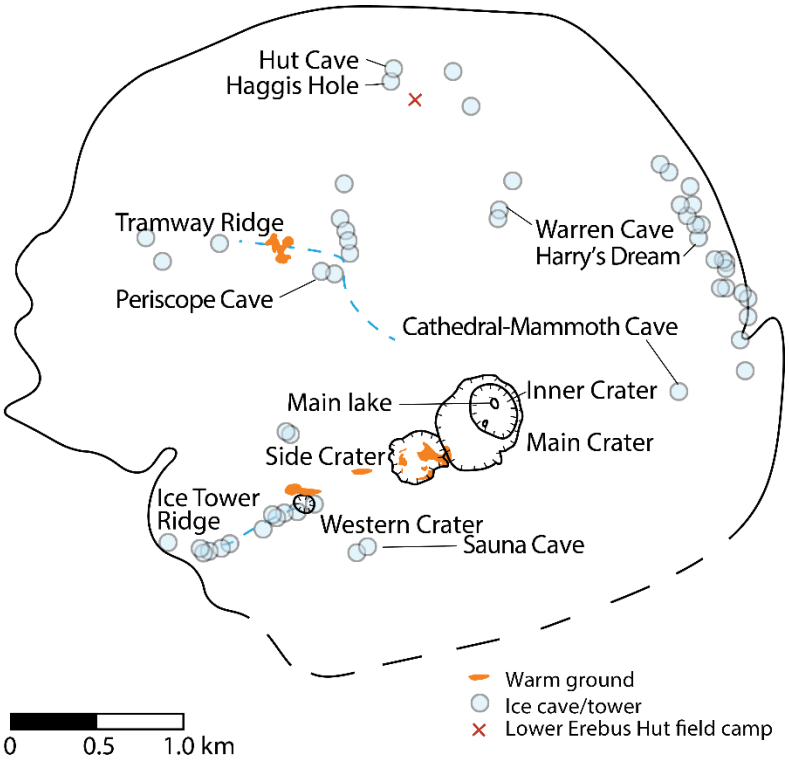

Figure 2. Erebus caldera, with craters, major ice towers, and ice caves. Warm ground areas include areas around Tramway Ridge (dashed line), Western Crater, and Side Crater. Data from Panter and Winter (2008)*, Curtis and Kyle* (2010)*, and field observations.*

Erebus is perhaps best known for the long-lived phonolite lava lake in its summit cone. This cone rises from a plateau on the upper flanks of the volcano, formed by two overlapping calderas at about 3400 m altitude, which contains over 100 FIC. Descriptions of many of these FIC, reported over several expeditions, are available through the Erebus caves database (Curtis and Kyle, 2010). At Erebus, the typical FIC is on the boundary between rock and snowpack, and not within a glacier, although it should be noted that ice density is closer to that of glacial ice than of firn (Curtis, 2015). A number of features of the caves are described by Curtis (2015) including barometric pumping at entrances, hot vents in the rock floors as well as cold vents on the surface through which outside air mixes in, and changes in the size and shape of caves between annual field seasons. Known areas of upper flank degassing on Erebus (Fig 2) include Ice Tower Ridge (ITR), a line of small FIC extending from the southwest of the plateau through areas of warm ground on the flanks of the summit cone, and terminating at Side Crater, itself containing a number of fumaroles and warm ground areas (Panter and Winter, 2008). Other areas of interest include Tramway Ridge, which is an Antarctic Specially Protected Area (ASPA) of warm ground to the northwest of the summit cone, and more extensive caves located at various sites around the plateau including Hut Cave to the north, Warren Cave (NE), the sometimes-connected Cathedral-Mammoth system (SE), and Sauna (S).

The active magmatic system at Erebus degasses through the lava lake(s) and nearby high temperature vents with a composition rich in CO_2 relative to water and SO_2 (Oppenheimer and Kyle, 2008). Melt inclusions in Ross Island basanites, which are considered representative of the parental melt for the Erebus phonolite, contain up to 1.8% CO_2 (Rasmussen et al., 2017). Degassing at shallow depths is controlled by the solubility of the various volatile species, but CO_2, which is relatively insoluble, may be sourced from the mantle

(Oppenheimer et al., 2011). Based on plume gas chemistry and melt inclusion volatile contents, deep degassing is likely to be the biggest contributor to the lava lake gas plume, followed by degassing from the lava lake, with limited input from intermediate regions (Iacovino 2015). At shallow depths, seismic tomography and interferometric studies by Zandomeneghi et al. (2013) identify several low- and high-velocity zones within hundreds of metres below the surface of the Erebus summit plateau. They suggest that these correspond to hot magma bodies or high permeability zones, and cooled intrusions or buried lava and caldera rim features, respectively. The complex shallow magmatic plumbing has been attributed to possible restriction of fluid flow by the latter. Both low- and high-velocity zones may influence the location of degassing features such as ice caves, and the nature of subsurface structures may be reflected in the gas measured at the surface.

Ice and snow cover are variable around the Erebus caldera. Only limited meteoric water recharge is possible in the arid climate, but localized melting of ice and snow, associated with heat from FIC and warm ground areas, is evident. Groundwater on the Antarctic continent includes brines beneath the permafrost in the Dry Valleys (Mikucki et al., 2015), and groundwater in ice-covered regions, where it may have some association with subglacial volcanism (Christoffersen et al., 2014). The nature of a hydrothermal system on Erebus has not been directly addressed before, although the presence of any substantial amount of liquid water within the volcanic edifice will have implications in assessing potential hazards.

Volcanic activity on Erebus has mostly been stable over the past century or more, dominated by passive degassing and small Strombolian explosions from the lava lake and adjacent vents. However, two significant phreatic eruptions occurred in October 1993, emitting debris described by Dibble et al. (1994) as hydrothermally altered. Evidence of phreatomagmatic activity in the Side Crater was found by Panter & Winter (2008) and attributed to melting from the surface or permafrost, or to shallow hydrothermal water. Distal tephra layers indicate that frequent phreatoplinian eruptions have occurred in the past (Harpel et al., 2008; Iverson et al., 2014) but these have been explained as a result of snow or ice accumulation within the crater.

Here, we report gas compositions, carbon isotope and nitrogen isotope data, and CO_2 fluxes, which reflect sources of degassing and modification by crustal or hydrothermal processes. Wardell et al. (2003) previously investigated CO_2 fluxes and carbon isotope ratios at ice towers and warm ground areas, suggesting that the measured carbon isotope ratios are due to mantle CO_2 sources, but without accounting for the range of observed values. While a heterogeneous mantle source is one possibility, other processes such as dissolution in water may also affect CO_2 degassing and carbon isotope composition. If magma bodies in the upper 400 m of the volcanic edifice influence degassing, then we expect compositions of gases emitted above hot intrusions as identified by Zandomeneghi et al. (2013), where a magmatic signature is likely, to differ from those emitted above cooled intrusions, where gases are potentially more deeply sourced but follow old pathways, and are more susceptible to mixing with surface air or dissolution in meltwater.

2. Methods

2.1 Gas sampling

Samples were collected at vents or diffuse degassing sites, within caves and in warm ground areas. We focused on sites that were known to have been entered in the past, due to the biological sensitivity of pristine and little-visited caves. For gas composition, argon and nitrogen isotope analyses, samples were collected in copper tubes and Giggenbach bottles (Giggenbach, 1975). Air samples were also collected inside and outside caves, generally by opening a pre-evacuated vial or Giggenbach bottle. These provide samples for background compositions. Samples for carbon dioxide isotope analyses were taken in 1L Tedlar bags for analysis at the field camp with an infrared isotope ratio spectrometer.

Soil probe and titanium tubes

Samples were mostly collected using a 5V battery-powered pump, and a soil probe or titanium tube, connected to sampling vessels by tygon tubing. The soil probe or tube was inserted as far as possible into soil or gravel on the cave floors where temperatures were elevated, or into cracks in the rock where degassing was observed. Typically, sampling vessels included a series of four 30 cm lengths of soft copper tubes with about 6 mm internal diameter, linked by short sections of tygon tubing. One end of this sample train was connected to a 1 m soil probe, and the other to the intake of the pump. The pump outlet could be connected to a needle that injected gas through the seal into a pre-evacuated 10 ml glass vial, with a second needle inserted into the seal to maintain gas flow through the vial. In some instances, gas flow out from the vent was sufficient that no pump was required. The highest airflow velocity from a vent was measured by an anemometer at over 6 $m \cdot s^{-1}$ (Shooting Gallery, Ice Tower Ridge).

The pump and soil probe setup was left for several hours, and usually for one day, to flush out ambient air, with the exception of high temperature sites at Sauna and Tramway (measured in 2016) where they were collected after one hour. The battery and pump could operate for several days if required so that samples were not lost in case a return to the site was delayed by bad weather. For collection, we removed the needles from the vial, and cold-welded the ends of the copper tubes while they remained connected to the soil probe.

Accumulation chamber

To measure soil CO_2 fluxes, we used a PP Systems accumulation chamber (SRC-1), connected to a portable CO_2 analyser (EGM-4) with an internal pump and rechargeable NiMH battery. The analyser logs CO_2 flux and concentration, and the outlet could be connected to a bag to collect soil gas samples (Lee et al., 2016). The analyser automatically calculates fluxes based on the rise in concentration, for which we specified a linear fitting. We assume there is a linear increase in CO_2 concentration within the cylindrical chamber volume due to constant gas flux. The rate of change in CO_2 concentration over the chamber area (calculated over two minutes for the EGM-4, unless fluxes are high), multiplied by the chamber height then gives the CO_2 flux (Chiodini et al., 1998). Non-linear results generate an error while recording, but wherever all concentration data were saved they have also been checked manually to ensure linear increases in CO_2 concentrations.

Tedlar bags

The Tedlar bags used for CO_2 collection and analyses are of impermeable and flexible polyvinyl fluoride, with a plastic valve. Samples in ice caves and warm ground were collected by attaching a bag either to the outlet of the accumulation chamber used for CO_2 flux measurements, or to the outlet of a pump box being used to

collect copper tube samples. For lava lake plume and summit fumarole samples, we used 100 mL syringes to draw in air and expel it into the valve, repeating the process several times for each bag, with two samples also collected via the outflow of a MultiGas instrument. These samples are expected to contain a significant proportion of ambient air. Clean ambient air and ambient air next to Lower Erebus Hut (LEH) were also collected using a syringe, while ambient air at Tramway Ridge and within caves were collected by connecting to a pump. Samples were analysed with the isotope ratio spectrometer set up at LEH, usually within 48 hours of collection (section 2.2).

2.2 Isotope ratio infrared spectrometer

Carbon dioxide isotope ratios were measured using a tunable-laser isotope ratio infrared spectrometer (IRIS); specifically, the Thermo-Fischer Delta Ray. As in a conventional closed-path infrared spectrometer, the sample gas is passed into an internal cell where it absorbs infrared radiation and the resulting energy spectrum is measured. The absorption wavelengths shift according to the carbon and oxygen isotopes involved, such that peaks on the measured spectrum reflect the proportions of these isotopes. For the Delta Ray, a tunable-laser inside the instrument is the radiation source, targeting the 4.3 μm absorption band. Fitting parameters, including the peaks to be fit, can be specified, and the software uses the HITRAN database (Rothman et al., 2013) as a reference; we used the default settings for CO_2 in air. Using the sizes of and shifts in absorption peaks, the built-in software, Qtegra, calculates the isotope ratios of the sample. The results are referenced to calibration gases of a known composition, which were connected to reference gas intakes and diluted with zero air by the instrument to match the sample concentrations.

The instrument was set up inside a hut at Lower Erebus Hut field camp (LEH, elevation approx. 3400 m, ambient air pressure approx. 630 bar). Tedlar bags were connected to the sample intake via tygon tubing and a supplied steel capillary, generally following procedures described by Fischer and Lopez (2016). The sample was pumped into the cell by an internal vacuum pump. To maintain internal cell pressure at the required 100.0+/-0.1 mb, an altitude modification was required, in the form of a valve that constricted the tubing between the pump and cell port. For samples containing over 3500 ppm CO_2, dilution was carried out by adding CO_2-free air directly from a cylinder into the bags via tygon tubing. Starting concentrations were estimated from the volume change after dilution, or measured using the Delta Ray before dilution. Due to the possibility of contamination by ambient air during dilution, air sampled near the hut, which is shifted to lighter carbon isotope ratios due to emissions from the stove used for heating, is also reported. Samples were referenced to a Thermo Fisher reference gas with isotope ratios of -27.2 ± 2 ‰ $\delta^{18}O$ and -27.8 ± 2 ‰ $\delta^{13}C$.

2.3 Laboratory analyses

Gas compositional analyses were conducted for copper tube, Giggenbach bottle, and some vial samples, in the Volatiles Laboratory at the University of New Mexico following techniques most recently reported by Lee et al. (2017). Splits of the same sample were used for gas chromatography (GC) and quadrupole mass spectrometry. We used a Gow Mac GC with a discharge ionization detector, using a 5Å molecular sieve column with helium as the carrier gas, providing CO_2, $Ar+O_2$, N_2, CH_4, and CO. A Pfeiffer QMS was used in dynamic mode to measure He, Ar, O_2, and N_2. A liquid nitrogen trap was used to freeze out most water before QMS analyses; but as oxygen measurements from the QMS may still be affected by water the results given here use N_2 from the GC, and Ar and O_2 calculated as follows:

$Ar_{reported} = Ar_{QMS}/N_{2QMS} * N_{2GC}$

$O_{2reported} = (Ar+O_2)_{GC} - Ar_{reported}$

Helium amounts in most samples were low (<60 ppm). Argon isotope ratios were obtained by using the QMS to measure masses 36, 38, and 40 in static mode, after a liquid nitrogen trap and a charcoal trap at 550°C, following Lee et al. (2017).

Compositional analyses showed variability between copper tube samples collected from the same soil probes at almost the same time, which may be due to variations in the level of air contamination. Two possible causes of air contamination are: (1) that air was mixed in during crimping of copper tubes, (2) that cave air, rich in CO_2 and otherwise similar to outside air, is held in the shallow soil and gravel and pumped into our sample set up, but is displaced by intermittent puffs of pristine gas. Most break seal sample splits for nitrogen isotope analyses were therefore prepared from the same copper tubes analysed by GC-QMS. The copper tube was attached to a valve which connected to the vacuum line and a borosilicate break seal at a three-way connection. After evacuating the break seal, a split was taken for GC-QMS analyses, and the copper tube was opened a second time to the break seal to increase the sample pressure, before torching it off. Nitrogen isotope analyses were conducted by isotope ratio mass spectrometry, following de Moor et al. (2013). Air standards in glass break seals were run every 3-4 analyses as references to correct raw values ($\delta^{15}N = 0$ ‰). A blank was also run for each sample or air standard before breaking it, with the peak areas subtracted from those subsequently measured in the sample or standard run. The blank-corrected air values were subtracted from the blank-corrected sample values. Reported errors are given in 1 s.d. over 4-6 peaks. Although the number of peaks for calculations varies between samples, the same peak numbers were used for the blank corrections and the air standard associated with each sample. Samples collected in 2012 were analysed for carbon and some noble gas ($^3He/^4He$ and $^4He/^{20}Ne$) isotope ratios at the University of Tokyo (Sano et al., 2008)

3. Results

3.1 Gas chemistry

Gas analyses from the GC-QMS (Table 1) show that most samples have air-like compositions. The main differences between samples are in their CO_2, O_2, and N_2 contents (Fig 3). Helium is up to a few tens of ppmv above air, reaching 99 ppm for a sample collected at Warren Cave in 2012. Hydrogen (H_2) and methane concentrations are below 0.1%, and CO below 0.2%. Other hydrocarbons may be present, and a fuel-like smell was observed in parts of Warren Cave, but these cannot be measured using our current methods. CO_2 contents are below 2.9%, with four samples containing less CO_2 than ambient air on Erebus. The lowest CO_2/CO ratio measured is 0.5, at Ice Tower Ridge in 2016, while at other sites, CO is not detectable.

Of the potentially air-derived components, nitrogen varies from about 76% to up to 99%, while oxygen is typically close to or less than 21% down to <1% (with a few samples up to 24%), and argon from 0.5% to 1.3%. There is no clear trend in the relationship between these components; low oxygen samples occur across a range of N_2/Ar ratios. High CO_2 concentrations occur both in samples where N_2/Ar and N_2/O_2 ratios resemble air, and in those that are oxygen-poor.

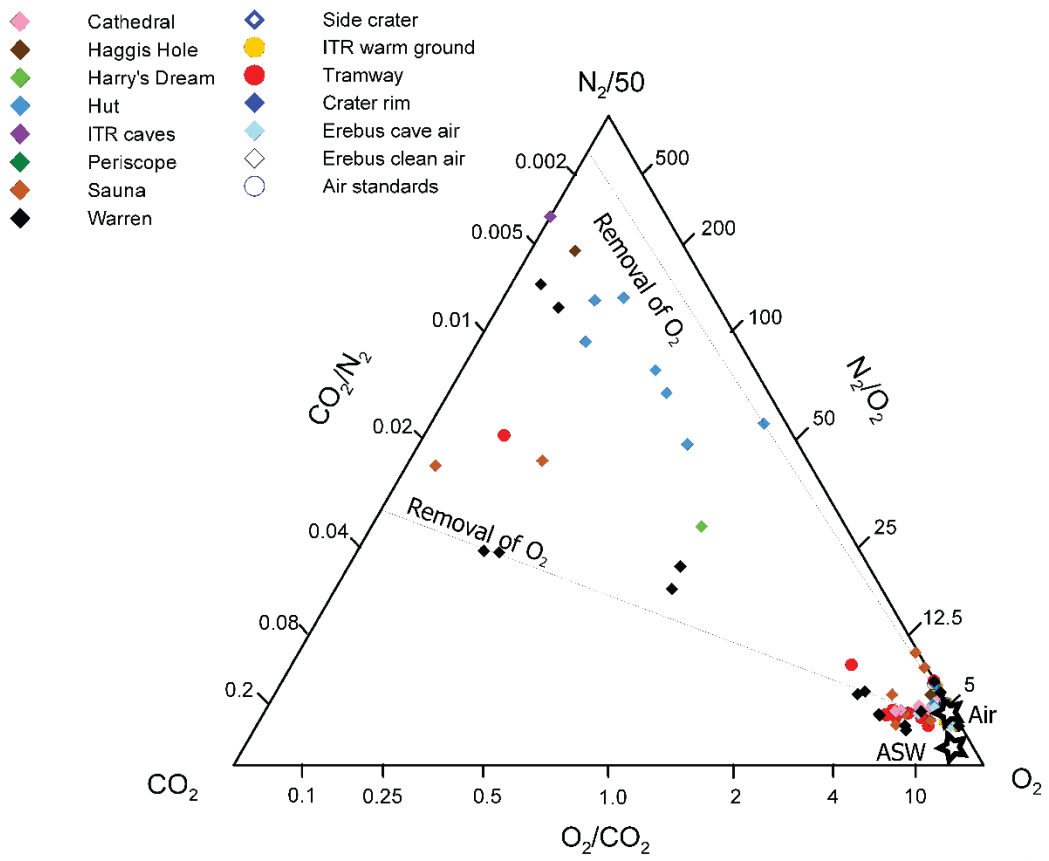
Cathedral
Haggis Hole
Harry's Dream
Hut
ITR caves
Periscope
Sauna
Warren
Side crater
ITR warm ground
Tramway
Crater rim
Erebus cave air
Erebus clean air
Air standards
N2/50
CO2/N2
N2/O2
CO2
O2
O2/CO2
Removal of O2
Removal of O2
Air
ASW
0.002
0.005
0.01
0.02
0.04
0.08
0.2
500
200
100
50
25
12.5
5
0.1
0.25
0.5
1.0
2
4
10

a

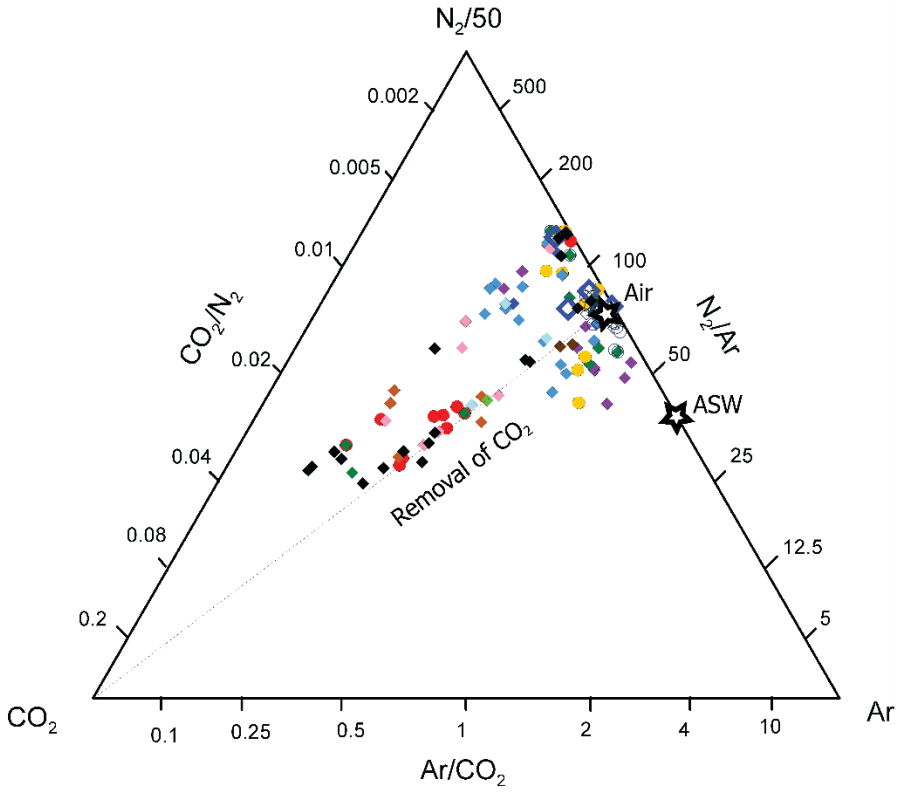
N2/50
CO2/N2
N2/Ar
CO2
Ar
Ar/CO2
Removal of CO2
Air
ASW
0.002
0.005
0.01
0.02
0.04
0.08
0.2
500
200
100
50
25
12.5
5
0.1
0.25
0.5
1
2
4
10

b

315

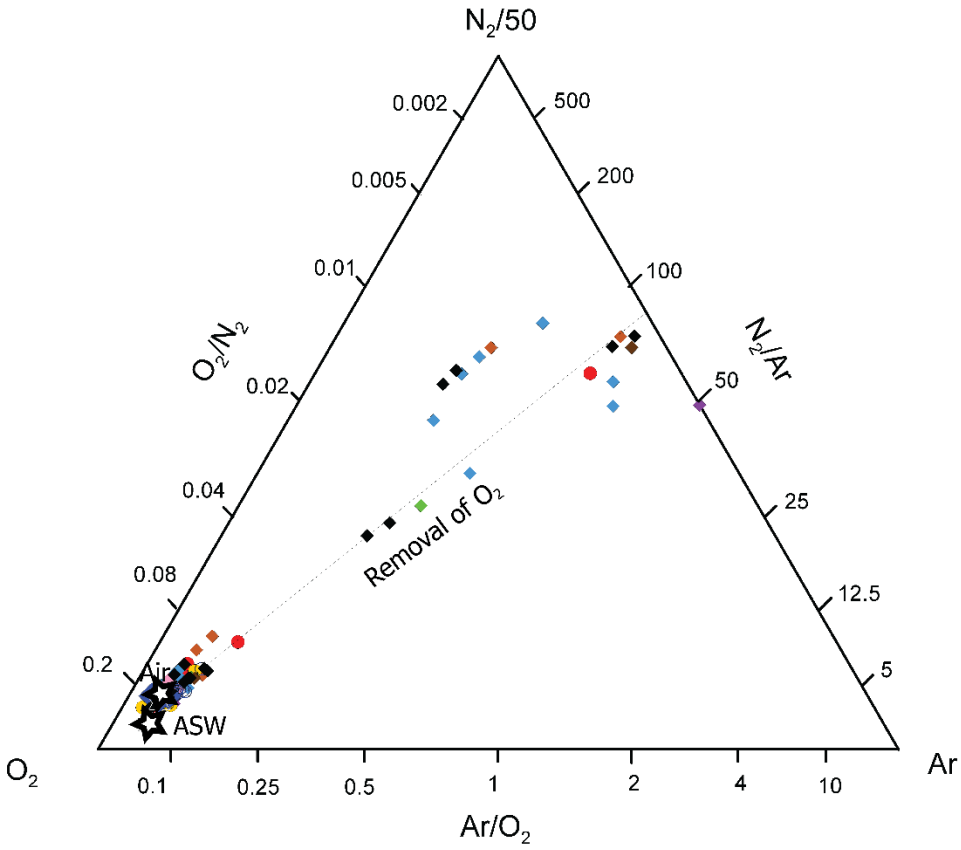
N2/50
0.002
0.005
0.01
0.02
0.04
0.08
0.2
O2/N2
500
200
100
50
25
12.5
5
N2/Ar
Removal of O2
Air
ASW
O2
0.1
0.25
0.5
1
2
4
10
Ar
Ar/O2

c

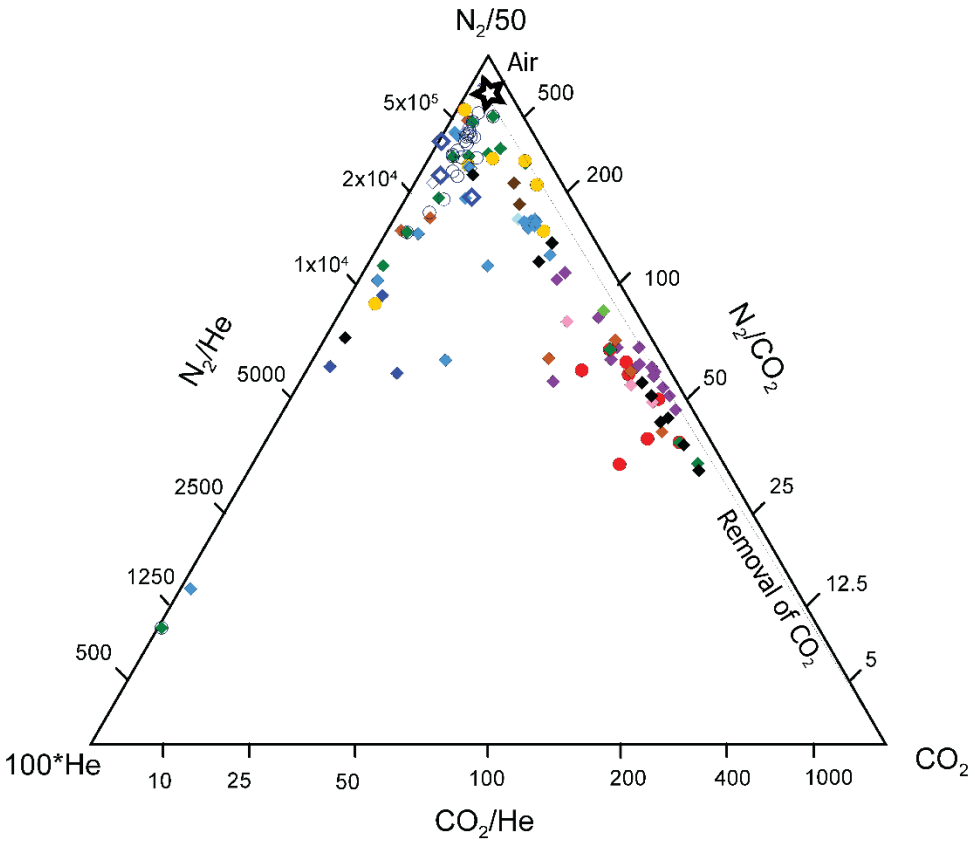
N2/50
Air
5x10⁵
2x10⁴
1x10⁴
5000
2500
1250
500
N2/He
500
200
100
50
25
12.5
5
N2/CO2
Removal of CO2
100*He
10
25
50
100
200
400
1000
CO2
CO2/He

d

316

Figure 3. Ternary plots of (a) CO_2-N_2- O_2, (b) CO_2-N_2-Ar, (c) O_2-N_2-Ar, (d) He-N_2-CO_2 measured in 2012, 2015, and 2016 field seasons by GC-QMS.

The samples taken at Hut Cave show that measurements at one site may vary significantly, and as mentioned in section 2, analyses of duplicate copper tubes from the same sampling setup can show differing degrees of air contamination. This includes sites where gas flow out was known to have high CO_2 flux (e.g. Tramway, Sauna) or to be concentrated (such as sites at Ice Tower Ridge and Hut Cave), and we thus consider this to be a result of unsteady flow, at least in some cases, rather than contamination during sampling.

3.2 Isotope ratios

Carbon isotope ratios (Fig 4) are mostly between -2‰ and -6‰. Mixing lines through clean Erebus air or air contaminated by stove exhaust from the hut generally project to a range of values between -1‰ and -4‰ at pure CO_2, and one 2012 sample from Tramway (Table 3) projects to -4.8‰ on a mixing line with 2016 outside air. The time series of samples collected into Tedlar bags at Hut Cave (Fig 5) shows very consistent results, both in concentration and in $\delta^{13}C$ values.

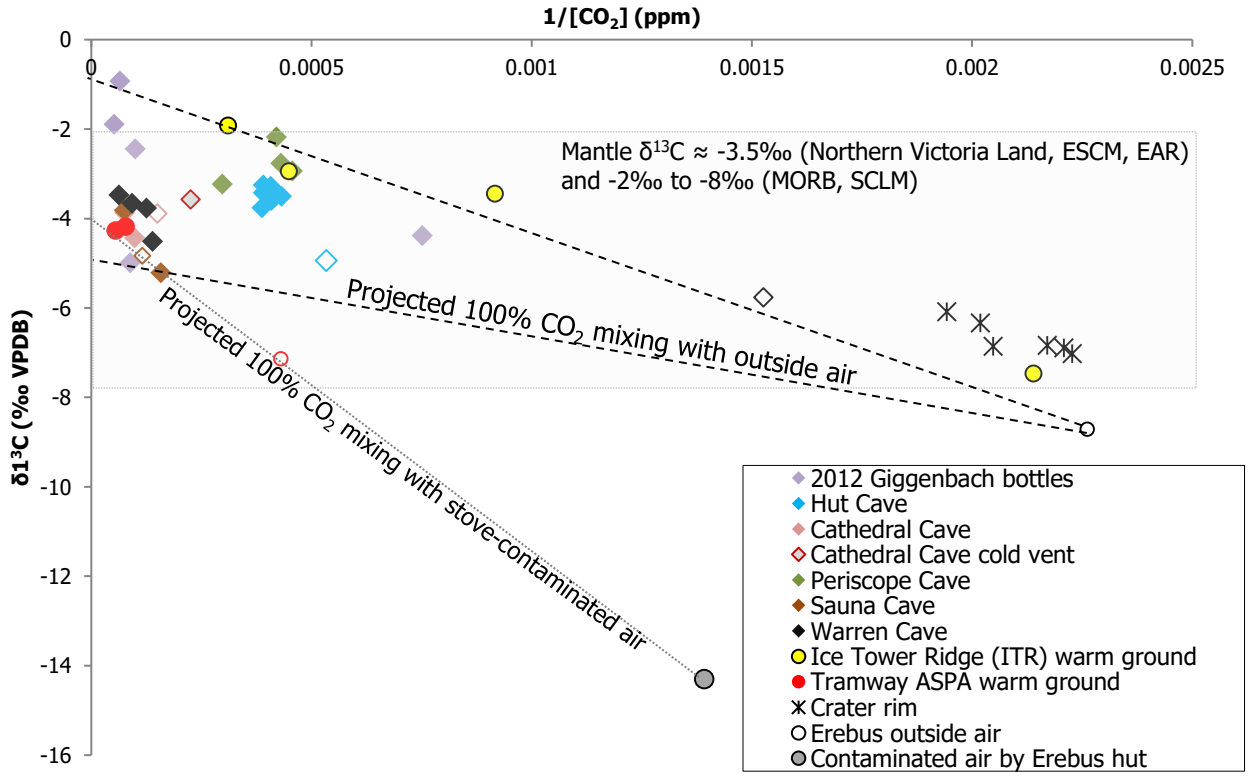

Figure 4. Carbon isotope ratios from Erebus 2016 field season tedlar bag samples measured by Delta Ray, and from 2012 measured by conventional IRMS. Hollow symbols represent ambient air sampled at cave entrances or above warm ground area. Mantle $\delta^{13}C$ are: -3.5‰ for Northern Victoria Land Subcontinental Lithospheric Mantle (Correale et al. 2017), European Subcontinental Mantle (Bräuer et al., 2016), and East African Rift (Lee et al., 2016); -2 to -8‰ SCLM-derived xenoliths (Cartigny, 2005); -5±3‰ MORB (Fischer and Chiodini, 2015)

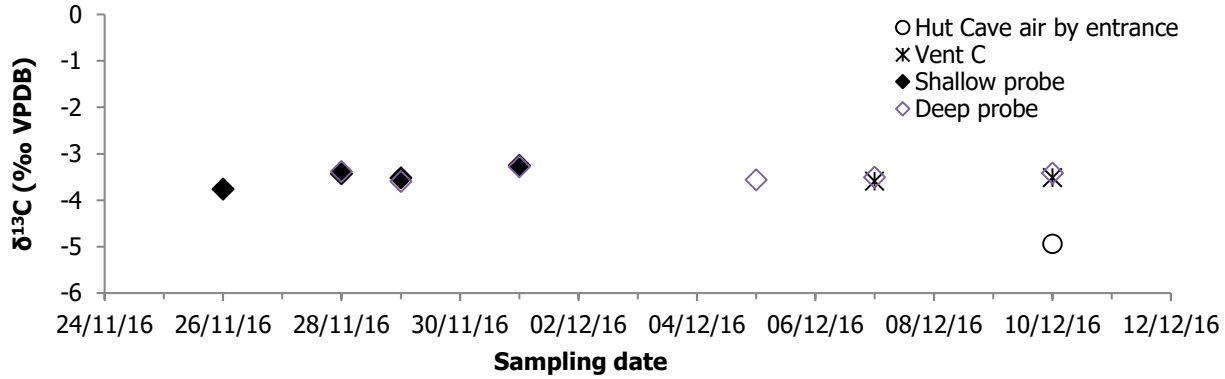

342
343 *Figure 5. Time series of carbon isotope ratios collected in Tedlar bags in Hut Cave, measured by Delta Ray*
344

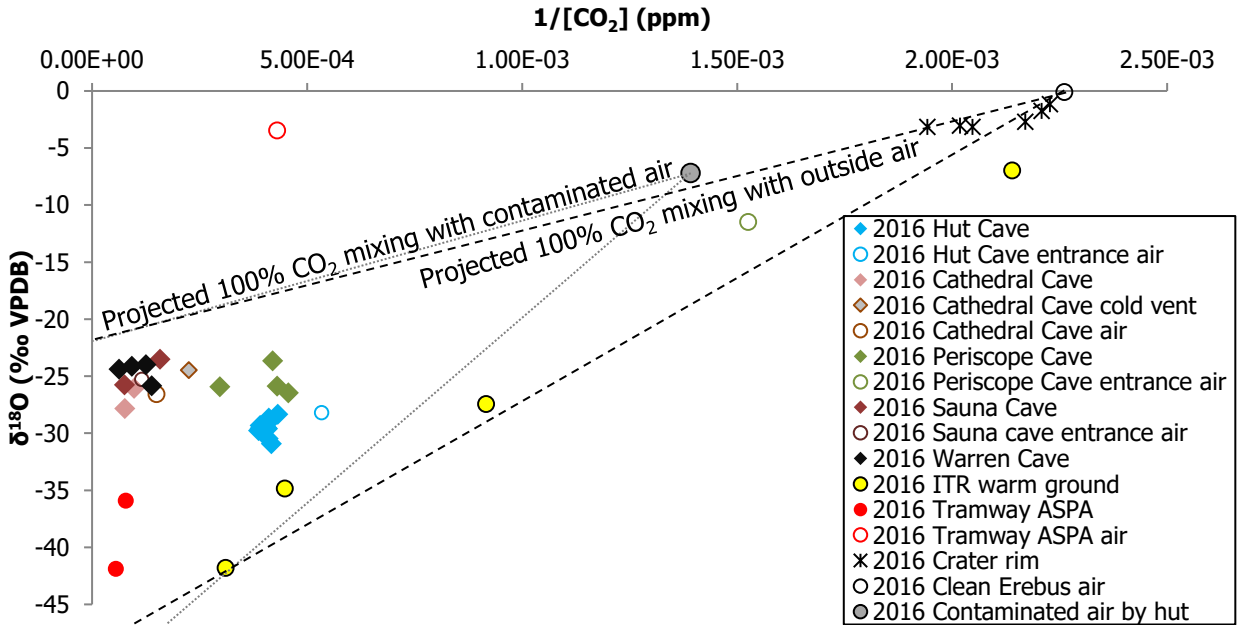

345
346 *Figure 6. Oxygen isotope ratios of CO_2 from Erebus 2016 field season measured by Delta Ray. Symbols as for figure 3.*
347

348 Oxygen isotope ratios of CO_2 measured by Delta Ray (Fig 6) also vary with $\delta^{13}C$, and lighter oxygen isotope
349 ratios are associated with warm ground areas, while cave vent samples are mostly in the -20 to -30‰ range.

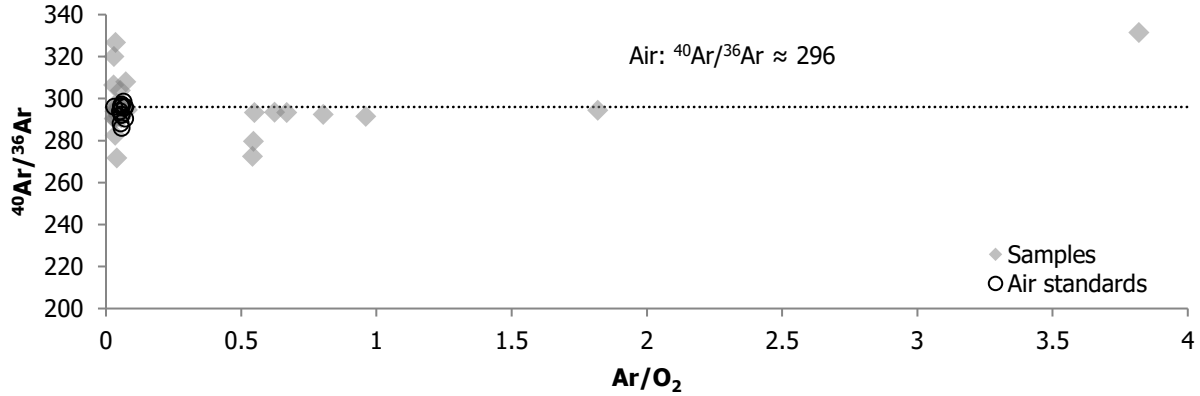

350
351 *Figure 7. $^{40}Ar/^{36}Ar$ from 2015 and 2016 samples and laboratory air, measured by QMS.*

Argon isotope ratios (Fig 7), measured on the QMS, range from 272 – 331, which is generally in the range measured for our internal air standard ($^{40}Ar/^{36}Ar$ =286 – 308). The highest value of 331 corresponds to a sample from Hut Cave (HUT-shallow-14), which has the highest N_2/Ar ratio and very little O_2.

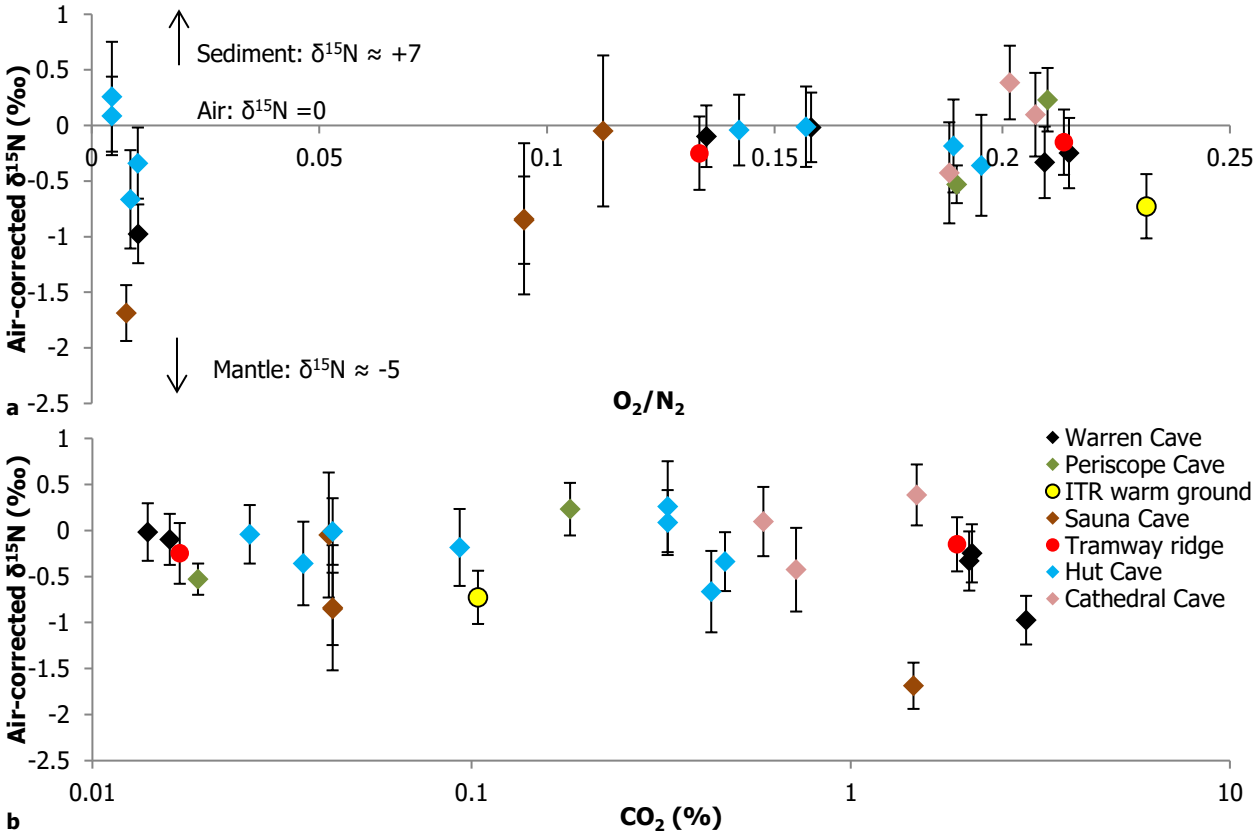

Figure 8. (a) Nitrogen isotope ratios from IRMS vs. O_2/N_2 ratios measured by GC-QMS; (b) Nitrogen isotope ratios vs. CO_2 (%) measured by GC-QMS. Symbols as for figure 3.

Nitrogen isotopes range from -1.7 – +0.4‰ vs air, with 1 s.d. up to 0.6‰ (Table 1, Fig. 8), after recalculating the variance to include standard deviations of air standards used to correct measured raw values from IRMS. The lightest of these values are outside of the range expected for air. Helium isotope ratios (Table 3) are just above those expected for air, with a range of 1.03 – 1.18 R_a.

367 *Table 1. Summary of gas data from laboratory analyses (GC-QMS and IRMS); italics indicate ambient air samples (not pumped); < indicates peaks visible on GC but*
368 *amounts below software detection thresholds.*

Type	Sample ID	Site	Gas composition (vol %) from GC-QMS								QMS (static)	IRMS		
			CO_2	He	H_2	Ar	O_2	N_2	CH_4	CO	$^{40}Ar/^{38}Ar$	Sample ID	$\delta^{15}N$	1
2012 Cu tubes	EBG-2b	Haggis Hole	0.37	0.0017	0.0005	1.28	0.15	98.20	0.0007	<				
	EBG-20	Sauna	2.09	0.0023	0.0012	1.15	0.16	96.57	0.0005	0.016				
	EBG-14	Tramway	1.08	0.0013	<	0.87	22.33	75.72	0.0011	<				
	EBG-13	Warren v2	0.60	0.0024	0.0004	1.19	0.23	97.99	<	<				
	EBG-9	Warren v5	1.84	0.0013	<	0.90	21.48	75.78	<	<				
	EBG-10	Warren v6	0.06	0.0099	<	0.89	23.42	75.62	<	<				
	EBG-12	Warren v7	2.09	0.0013	<	0.86	23.75	73.30	<	<				
	EBG-11	Warren v8	0.58	0.0015	0.0004	1.23	0.10	98.09	<	<				
2012 Giggenbach bottles w. caustic	EBG-11	Warren v8	0.00	0.0016	<	1.03	13.99	84.98	0.0001	<				
	EBG-9	Warren v5	0.00	0.0013	<	1.06	13.78	85.17	<	<				
	EBG-12	Warren v7	0.00	0.0017	<	1.04	13.79	85.17	<	<				
	EBG-13	Warren v2	0.00	0.0014	<	1.02	14.62	84.36	<	<				
	EBG-15	Harry's Dream	0.00	0.0010	<	1.05	13.62	85.33	<	<				
	EBG-20	Sauna	0.00	0.0016	<	1.03	13.97	85.00	0.0003	<				
	EBG-14	Tramway	0.00	0.0007	<	0.97	13.64	85.39	0.0017	<				
2012 Air standards	*Crest air*	*Sandia crest*	*0.05*	*0.0009*	*0.0006*	*0.97*	*17.67*	*81.31*	<	<				
	Crest air	*Sandia crest*	*0.06*	*0.0015*	<	*0.97*	*17.56*	*81.42*	<	<				
	Crest air	*Sandia crest*	*0.05*	*0.0012*	<	*0.96*	*17.62*	*81.37*	<	<				
	Crest air	*Sandia crest*	*0.05*	*0.0014*	<	*0.94*	*17.46*	*81.54*	<	<				
2015 Cu tubes	TR1	Tramway	1.47	0.0020	0	1.23	0.41	96.89	0.0020	0.0010				
	HUT1	Hut	0.44	0.0019	0	1.40	0.34	97.82	0.0010	0.0020				
												HUT-2B_2015	-	0.43
	SCR1	Side Crater	0.01	0.0022	0	1.04	18.37	80.58	0	0				
												SCR-2B_2015	-	0.58
	ITR-B-1	Shooting gallery 'blob'	0.05	0.0046	0	0.95	20.06	78.93	<	0				
	ITR-KM-1	Shooting gallery main	0.13	0.0013	0	0.83	20.36	78.67	<	0				
	ITR-UWG-11	ITR upper warm ground	0.02	0.0013	0.0010	0.99	12.56	86.43	0.0010	0.0020				
												ITR-UWG-12_2015 B	0.05	0.61
	DDNOS	Hollow near Derodrome	0.15	0.0009	0.0000	1.17	20.89	77.79	<	<				
	ITR-UWG-6	ITR upper warm ground	0.41	0.0012	0	1.42	21.11	77.06	<	<				
	ITR-H-1	Heroin	0.14	0.0013	0	1.01	21.24	77.61	<	<				
												ITR-H-2B_2015	-	0.31
	ITR-LWG-1	ITR lower warm ground	0.29	0.0006	0	1.20	21.35	77.15	<	<				
	ITR-B-6	Shooting gallery 'blob'	0.36	0.0008	0	1.98	0.00	97.66	<	0.0010				
												ITR-B-7A_2015	0.21	0.12

											ITR-B-7B_2015	-	0.30
	ITR-P-1	Passage by Shooting	0.13	0.0005	0	1.46	20.58	77.83	<	0.0020			
	ITR-TOM-1	Tomato cave	0.06	0.0006	0	1.38	20.91	77.65	<	<			
	ITR-B-16	Shooting gallery 'blob'	0.23	0.0007	0	1.27	21.15	77.35	<	<			
	ITR-B-11	Shooting gallery 'blob'	0.23	0.0005	0	1.23	20.41	78.13	<	<			
	ITR-B-13	Shooting gallery 'blob'	0.23	0.0011	0	1.17	20.94	77.65	<	<			
	ITR-B-A	Shooting gallery 'blob'	0.23	0.0006	0	1.10	19.88	78.79	<	<			
	ITR-UWG-1	ITR upper warm ground	0.23	0.0005	0	1.18	19.80	78.80	<	<			
	ITR-B-12	Shooting gallery 'blob'	0.23	0.0005	0	1.29	18.96	79.52	<	<			
	HUT-3-2015	Hut	0.43	0.0043	<	0.67	0.83	98.06	0.0010	0.0010	292.36	HUT-3_2015	- 0.32
	TR-3-2015*	Tramway	0.02	0.0013	0.0010	0.71	11.69	87.58	0.0020	0.0030	294.97	TR-3_2015	- 0.24
												TR-2B_2015	- 0.27
	ITR-KP-2 2015	Shooting gallery	0.23	0.0014	0.001	0.59	19.11	80.06	<	<	290.42		
	ITR-B-8 2015	Shooting gallery 'blob'	0.34	0.0018	<	0.59	19.18	79.89	<	<			
	ITR_UWG_13 2015	ITR upper warm ground	0.01	0.0026		0.63	15.88	83.47		0.0010			
	SCR_3 2015	Side Crater ice tower	0.05	0.0077		0.59	18.63	80.71		0			
2015 Giggenbach bottles	*LEH air 9Dec 15*	*LEH*	*0.05*	*0.0016*	*0*	*1.16*	*18.28*	*80.51*	*0*	*0*			
	TR6	Tramway	1.01	0.0032	0	0.92	19.04	79.03	0.0010	0			
	ITR-LWG	ITR lower warm ground	0.09	0.0080	0	0.92	19.37	79.61	0	0			
	SCR8	Side Crater	0.16	0.0025	0.0010	0.89	19.29	79.66	0	0			
	SCR9	Side Crater	0.05	0.0028	0	0.88	19.78	79.28	0	0			
	LEH air 10dec15	*LEH*	*0.04*	*0.0032*	*0*	*0.87*	*19.30*	*79.78*	*0*	*0*			
2015 air standards	*Johnson field air*	*Johnson field*	*0.03*	*0.0005*	*0*	*1.23*	*16.43*	*82.31*	*0*	*0*			
	Johnson field air	*Johnson field*	*0.04*	*0.0005*	*0*	*1.12*	*18.21*	*80.63*	*0*	*0*			
	Johnson_air	*Johnson field*	*0.03*	*0.0006*	*0*	*1.18*	*17.44*	*81.34*	*0*	*0*			
	Johnson_air	*Johnson field*	*0.03*	*0.0005*	*0*	*1.15*	*17.64*	*81.18*	*0*	*0*			
2016 Cu tubes	HUT-1	Hut	0.11	0.0021	0	0.79	13.71	85.39	0	0	303.82		
	Hut-2*	Hut	0.58	0.0096	<	0.75	1.41	97.25	0	0	279.56		
	HUT-7	Hut	0.39	0.0016	0	0.54	16.70	82.38	0	0	320.09		
	HUT-1-Deep	Hut	0.39	0.0014	0	0.68	17.03	81.89	0	0	326.74		
	HUT-7-Deep	Hut	0.38	0.0014	0	1.26	15.67	82.69	0	0	308.02		
	HUT-14-Shallow	Hut	0.61	0.0018	0	1.56	0.43	97.40	0	0	331.43		
	HUT-Shallow_15*	Hut	0.47	0.0016	0.0020	0.66	0.99	97.87	0.0020	0.0010		HUT-Shallow-15_2016	- 0.23
	HUT_Shallow_16*	Hut	0.04	0.0018	0	0.63	16.24	83.09	0.0010	0		HUT-Shallow-16_2016	- 0.32
	HUT-11-Deep	Hut	0.06	0.0075	0	1.05	15.83	83.05	0	0.0030	294.59		
	HUT-21-Deep	Hut	0.11	NA[1]	0.0070	1.29	1.64	96.89	0	0.0020	272.50		
	HUT-22-Deep*	Hut											
	HUT_deep_23*	Hut	0.33	0.0047	0	0.80	0.44	98.43	0.0010			HUT-deep-23A_2016	0.08 0.26
												HUT-deep-23B_2016	0.25 0.34
	HUT-27-Deep	Hut									287.29		
	HUT_deep_28*	Hut	0.04	0.0026	0.0010	0.64	13.47	85.84	0.0010	0.0020		*HUT-deep-28_2016*	- 0.26

	HUT-C-1	Hut - back	0.15	0.0026	<	1.11	20.91	77.82	<	0.0040			
	HUT-C-2*	Hut - back	0.09	0.0049	0.0010	0.61	15.80	83.49	0.0020	0.0010		HUT-C-2_2016	- 0.29
	HUT-C-4*	Hut - back	0.03	0.0019	0	0.66	12.36	86.95	0.0010			HUT-C-4_2016	- 0.24
	CAT-A-1	Cathedral	1.49	0.0028	0.0010	0.67	16.42	81.41	0.0010	0.0010		CAT-A-1_2016	0.38 0.24
	CAT-A-2*	Cathedral	0.72	0.0014	<	0.68	15.63	82.97	0.0010	<		CAT-A-2_2016	- 0.32
	CAT-B-1	Cathedral	0.59	0.0026	0.0010	0.58	16.97	81.86	0.0020	<		CAT-B-1_2016	0.09 0.27
	CAT-B-4*	Cathedral	0.10	0.0019		0.64	14.51	84.75					
	ITR-UWG-1	ITR upper warm ground	0.10	0.0020	0.0010	0.73	18.61	80.34	0.0010	0.21	294.84		
	PER-A-2 before torching	Periscope	0.02	0.0018	0.0010	0.59	15.87	83.51	0.0010	0.0010	294.17	PER-A-2_2016	- 0.23
	PER-B-2 before torching	Periscope	0.18	0.0017	0.0010	0.49	17.23	82.09	0.0010	0	306.44	PER-B-2_2016	0.23 0.22
	Sauna-A-1	Sauna hot vent	0.04	0.0014	0.001	0.64	10.03	89.28	0.0020	<	293.98	Sauna-A-1_2016	- 0.48
	Sauna-A-2*	Sauna hot vent	1.46	0.0018	0.0010	0.68	0.73	97.12	0.0010	0.0020	291.57	Sauna-A-2_2016	- 0.18
	Sauna-B-1	Sauna cool vent	0.10	0.0041	<	0.61	16.35	82.94	<	0			
	Sauna-B-3*	Sauna cool vent	0.04	0.0057	0.0010	0.68	8.61	90.66	0.0010	0.0010	294.55	Sauna-B-3A_2016	- 0.39
												Sauna-B-3B_2016	- 0.28
	Warren entrance air	*Warren*	*0.82*	*0.0030*	*0.001*	*0.56*	*17.18*	*81.43*	<	<	295.64	ITR-UWG-1_2016	- 0.21
	WAR-v6-1	Warren	2.05	0.0013	0.001	0.56	16.86	80.53	0.001	<	293.97	WAR-v6-1_2016	- 0.24
	WAR-v6-2*	Warren (v6 2012?)	0.05	0.0067		0.61	18.01	81.32			291.13		
	WAR-vT-1	Warren far back	2.81	0.0015	0.0020	0.61	1.11	95.47	0.001	0.0010	293.41		
	WAR-vT-2*	Warren far back	2.09	0.0020	<	0.64	17.19	80.08	<	0	293.32	WAR-vT-2_2016	- 0.22
	WAR-vT-3*	Warren far back	0.01	0.0033		0.66	13.55	85.77			291.60	*WAR-vT-3_2016*	- 0.22
	WAR-CD-1	Warren icy chamber	2.90	0.0013	0.0010	0.61	0.98	95.51	0.0010	0.0010	293.46	WAR-CD-1_2016	- 0.12
	WAR-CD-2*	Warren icy chamber	0.02	0.0037	0	0.66	11.81	87.50			290.74	WAR-CD-2_2016	- 0.50
	TRAM-A-1	Tramway	1.51	0.0012	0.0020	0.64	16.07	81.77	0.0020	<	295.62		
	TRAM-A-4*	Tramway	1.20	0.0012	0.0020	0.88	17.26	80.64	0.0010				
	TRAM-B-1	Tramway	1.91	0.0015	0.0010	0.59	17.16	80.34	0.0090	<	290.21	TRAM-B-1_2016	- 0.22
2016 air standards	*Lab air*	*In lab*	*0.10*	*0.0025*	*0*	*1.31*	*16.58*	*82.01*	*0*	*0*	307.89		
	Lab air	*In lab*	*0.11*	*0.0017*	*0.001*	*1.08*	*16.84*	*81.96*	*0*	*0*			
	repeat	*In lab*	*0.07*	*0.0017*	*0.001*	*1.08*	*16.66*	*82.19*	*0*	*0*			
	Johnson field air	*Johnson field*	*0.08*	*0.0014*	*0*	*1.05*	*18.46*	*80.41*	<	*0*			
	Johnson field air	*Johnson field*	*0.08*	*0.0025*	*0*	*1.00*	*18.65*	*80.27*	<	*0*			
	Johnson field air	*Johnson field*	*0.08*	*0.0021*	<	*0.93*	*16.59*	*82.40*	<	*0*			
	Lab air	*In lab*	*0.10*	*0.0033*	*0*	*0.96*	*16.52*	*82.42*	*0*	*0*			
	Johnson field air	*Johnson field*	*0.06*	*0.0015*	*0*	*1.10*	*15.68*	*83.15*	*0*	*0*	295.96		
	Johnson field air	*Johnson field*	*0.06*	*0.0023*	<	*1.04*	*16.23*	*82.67*	<	*0*	298.60		
	Johnson field air	*Johnson field*	*0.06*	*0.0016*	*0*	*0.98*	*16.98*	*81.98*	*0*	*0*	286.01		
	Lab air	*In lab*	*0.06*	*0.0050*	*0*	*0.56*	*18.61*	*80.77*	<	*0*	296.08		
	Lab air	*In lab*	*0.08*	*0.0040*	*0*	*0.98*	*17.63*	*81.31*	*0*	*0*	291.57		
	Johnson Field air	*Johnson field*	*0.06*	*0.0017*	*0*	*1.02*	*17.18*	*81.74*	*0*	*0*	296.37		
	Johnson field air	*Johnson field*	*0.06*	*0.0020*	<	*1.01*	*17.33*	*81.60*	<	*0*	292.25		
	Johnson field air	*Johnson field*	*0.07*	*0.0015*	*0*	*1.03*	*16.13*	*82.77*	*0*	*0*			

	Johnson field air	*Johnson field*	*0.05*	*0.0023*	*0*	*1.10*	*16.12*	*82.72*	*0*	*0*	
	Johnson field air[1]	*Johnson field*	*0.04*	*0.079*		*0.70*	*17.89*	*81.29*			
2016 vials[1]	*HUT-entrance*	*Hut back*	*0.38*	*0.0013*	*0.0010*	*0.67*	*16.58*	*82.36*	*0*	*0.0030*	
	CAT_CaveAir[1]	*Cathedral*	*0.94*	*0.0037*	*0.001*	*0.58*	*18.07*	*80.40*	*0*	*0.0030*	
	CAT_CV	Cathedral cold vent	0.78	0.0025	0.0010	1.08	16.18	81.95	0	0.0030	
	Clean air by Cathedral-	*Outside cave*	*0.11*	*0.0019*	*0*	*0.93*	*23.18*	*75.78*	*0*	*0.00*	
	TRAM-A-5	Tramway	1.71	0.0028	0.0070	0.98	18.04	79.26	0	0.0020	
	TRAM-B-5	Tramway	1.82	0.0052	0.0010	1.02	17.11	80.04	0.0020	0.0030	
	Sauna cave air	*Sauna entrance*	*0.31*	*0.0016*	*0.0010*	*0.90*	*22.91*	*75.88*	*0*	*0.0020*	
	Sauna-A-5 vial	Sauna hot vent	2.09	0.0012	0.0010	0.76	20.87	76.28	0	0.0009	
	Sauna-B-5 vial	Sauna cool vent	0.82	0.0040	0.0020	0.96	20.24	77.96	0	0.0050	
	CAT-A-6 vial	Cathedral	1.49	0.0015	0.0010	1.02	16.58	80.89	0	0.0040	
	CAT-B-5 vial	Cathedral	1.30	0.0019	0.0020	1.01	16.32	81.35	0	0.0040	
	Vial: ITR-UWG 30 Nov	ITR upper warm ground	0.14	0.0012	0.0010	0.64	23.01	76.20	<	0.0030	
	WAR_CD_5_vial	Warren icy chamber	0.07	0.0018	0	0.69	16.48	82.75	0	0	
	Sauna_A_good_vial	Sauna hot vent	1.32	0.011	0.0010	0.60	17.29	80.77	<	0.0050	
	Low pump site 17:15	*Low pump site*	*0.35*	*0.011*	*0.0010*	*0.69*	*16.73*	*82.21*	*0*	*0.0020*	
	Low pump site 17:00	*Low pump site*	*0.08*	*0.013*	*0*	*0.67*	*16.92*	*82.32*	*0*	*0*	
	Low pump site 17:06	*Low pump site*	*0.10*	*0.0077*	*0.0010*	*1.10*	*16.43*	*82.36*	*0*	*0.0030*	
	Rim after exp 17:15	*Low pump site*	*0.08*	*0.0034*	*0.001*	*1.03*	*16.51*	*82.37*	*0*	*0.0020*	
	HUT_5_shallow vial	Hut	0.36	0.0016	0.058	0.98	16.13	82.47	0.0010	0.0020	

*Table 2. Helium isotope ratios for Cu tube samples in 2012; * indicates duplicates Cu tubes from the same sample setup as the previous sample; [1] Known or probable helium contamination from GC (copper tubes) or lab air (vials).*

Sample location	**$^{3}He/^{4}He$ (R_{atm})**	**$^{4}He/^{20}Ne$**
Harry's Dream	1.10	0.319
Tramway	1.08	0.313
Warren v7	1.05	0.319
Warren v6	1.03	0.316
Warren	1.18	0.320

372 *Table 3. Erebus CO_2 isotope ratios from analyses by IRMS (2012) and IRIS (Delta Ray, 2016)*

Sample ID	Date collected	$\delta^{13}C$ (‰)	$\delta^{18}O$ (‰)	$[CO_2]$ (ppm)
Cathedral				
CAT-cold vent[1]	09/12/2016	-3.57	-24.46	4,440
CAT-cave air[1]	09/12/2016	-3.89	-26.55	6,679
CAT-B-0[1,2]	09/12/2016	-4.43	-26.05	10,210
CAT-A-0[1]	09/12/2016	-3.87	-27.84	13,150
Harry's Dream[3]	2012	-2.44		10,010
Hut cave				
Hut 0 (shallow)	26/11/2016	-3.76	-29.76	2,52
HUT-6 (shallow)	28/11/2016	-3.43	-29.57	2,559
HUT-7 (shallow)	29/11/2016	-3.52	-29.51	2,464
HUT-13 (shallow)	01/12/2016	-3.25	-29.32	2,560
HUT-DEEP-0	28/11/2016	-3.38	-29.31	2,492
HUT-DEEP-1	29/11/2016	-3.60	-29.58	2,452
HUT-DEEP-6	01/12/2016	-3.28	-29.07	2,458
Hut Cave deep site	05/12/2016	-3.56	-29.04	2,438
HUT-DEEP-20	07/12/2016	-3.50	-28.33	2,315
HUT-DEEP-26	10/12/2016	-3.42	-28.68	2,434
HUT-C-0	07/12/2016	-3.59	-30.46	2,441
HUT-C-1[2]	10/12/2016	-3.51	-30.91	2,399
HUT-entrance air	10/12/2016	-4.94	-28.20	1,874
Periscope				
PER-AIR	03/12/2016	-5.77	-11.48	655
PER-A-0	02/12/2016	-2.18	-23.66	2,381
PER-B-0	02/12/2016	-2.77	-25.85	2,324
PER-B-1[2]	03/12/2016	-2.94	-26.46	2,197
PER-A-1	03/12/2016	-3.23	-25.91	3,363
Sauna				
Sauna-A-0[1]	04/12/2016	-3.82	-25.74	13,275
Sauna-B-0[1]	04/12/2016	-5.22	-23.51	6,320
Sauna-entrance air[1]	04/12/2016	-4.83	-25.28	8,660
Warren				
Warren v7[3]	2012	-1.89		19,321
Warren v6[3]	2012	-0.93		15,500
Warren[3]	2012	-4.38		
WAR-CD-0[1,*]	02/12/2016	-3.77	-23.99	8,000
WAR-v6-0[1,*]	30/11/2016	-3.47	-24.38	15,950
WAR-CD-0[1,*]	02/12/2016	-4.51	-25.85	7,200
WAR-v6-1[1,*]	02/12/2016	-3.66	-24.13	10,800
ITR-UWG				
ITR-UWG	30/11/2016	-7.46	-6.96	467
ITR UWG p63[2]	27/11/2016	-2.95	-34.84	2,231
ITR UWG 'fumarole' probe	30/11/2016	-1.92	-41.80	3,223
ITR-UWG p56	26/11/2016	-3.45	-27.44	1,091
Tramway				
Tramway[3]	2012	-4.99		11,386
TRAM-A-0[1]	05/12/2016	-4.18	-35.91	12,795
TRAM-B-0[1]	05/12/2016	-4.27	-41.87	18,160
Tramway air	05/12/2016	-7.14	-3.47	2,322
Rim				
Pump site via pump box 11:45	02/12/2016	-7.03	-1.16	448.9
Pump site via multigas outflow 12:00	02/12/2016	-6.84	-2.70	460.8
Rim - low pump site 16.50	08/12/2016	-6.86	-3.13	488.4
Rim - low pump site 16.58	08/12/2016	-6.34	-3.04	495.4
Rim - low pump site after explosion 17.15	08/12/2016	-6.90	-1.75	452.9
Rim - low pump site after explosion 17.10	08/12/2016	-6.09	-3.14	514.9
Clean air				
CAT-clean air	09/12/2016	-8.71	-0.08	442.3
Contaminated air outside garage				
Outside air	08/12/2016	-14.30	-7.17	718.4

373 * estimated concentration based on dilution volume
374 [1]diluted prior to analysis
375 [2]average of repeat measurements
376 [3]concentrations for samples analysed by IRMS are from corresponding GC-QMS analyses of Giggenbach bottles

3.3 Carbon dioxide fluxes

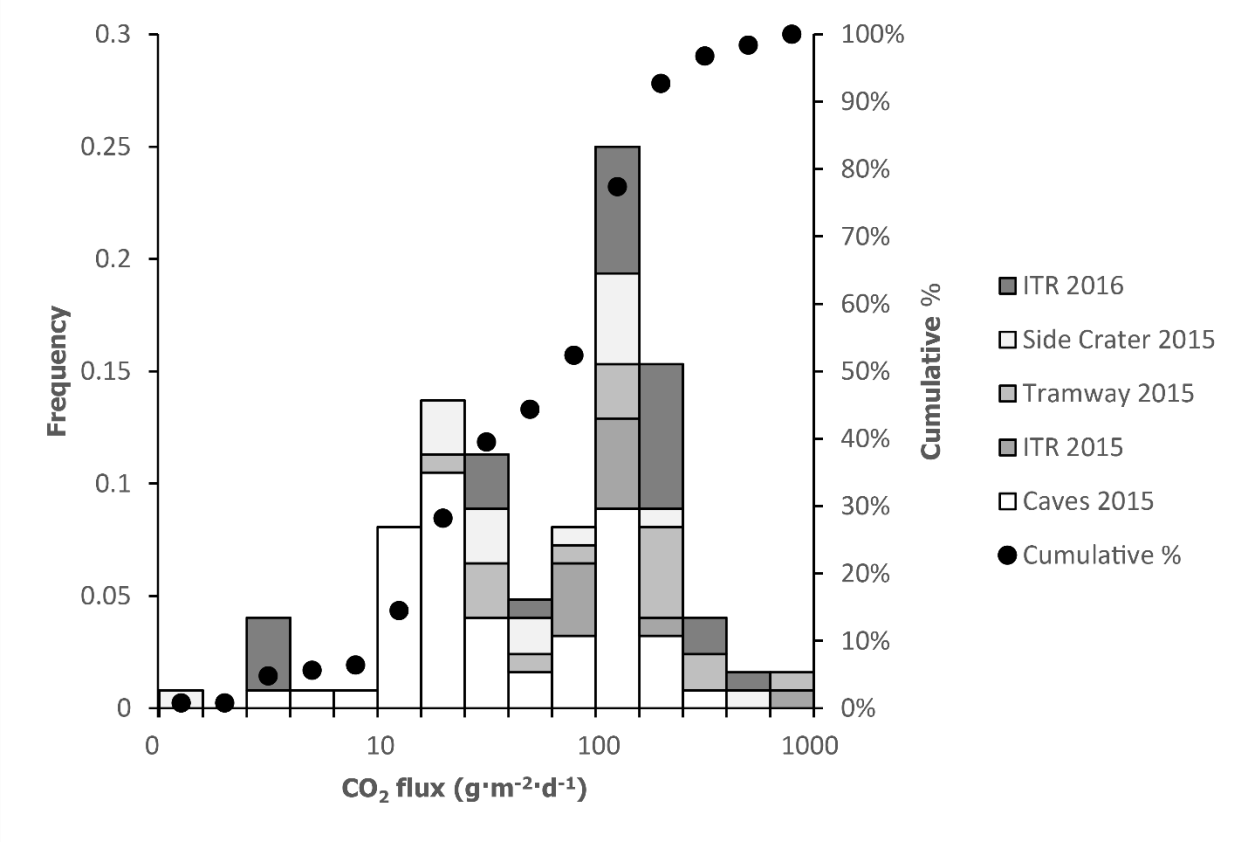

Figure 9. Population distribution of flux measurements taken in 2015 and 2016 at warm ground and cave sites.

Carbon dioxide fluxes measured in caves on Ice Tower Ridge (ITR) and the warm ground areas at ITR, Tramway, and Side Crater, seem to follow bimodal distributions (Fig 9). Fluxes were estimated for three warm ground sites based on their areas (Table 4), but do not include all such sites on the volcano due to time and access constraints.

Table 4. Summary of estimated CO_2 fluxes from warm ground areas

Warm ground site	Mean flux ($g \cdot m^{-2} \cdot d^{-1}$)	No. points	Median flux ($g \cdot m^{-2} \cdot d^{-1}$)	Area (m^2)	Total emissions (CO_2 $t \cdot d^{-1}$)
Side Crater	119.6	17	74.88	17453[1]	2.09
Tramway Ridge	289.8	17	149.5	17500[2]	4.28
ITR (2015)	199.5	11	149.3	9164[3]	1.83
ITR (2016)	195.8	36	154.6	9164[3]	1.79
All measured (2015)	201.5	45	121.0	44117	8.2

[1] *From map of Side Crater in Panton and Winter (2008) and field observations*

[2] *From satellite imagery and Tramway ASPA map (ASPA No. 175 management plan, 2014)*

[3] *Estimated from area of Western Crater from handheld GPS walk around limits of warm ground (8834 m^2) – and steeper upper warm ground areas where flux measurements were taken, estimated using tape measure (330 m^2).*

4. Discussion

4.1 Carbon dioxide

4.1.1 Carbon isotope ratios

Previous carbon isotope analyses of gas at Erebus by Wardell et al. (2003) found a range of $\delta^{13}C$ of -2.04‰ to -4.61‰. This was interpreted as an enriched signature from a mantle-derived component with $\delta^{13}C$ of -2.1‰ mixed with varying proportions of air. Our measured values overlap with these but have a greater range (-0.9‰ to -5.0‰ before accounting for mixing with air). This matches the -5±3‰ typical of MORB (Fischer and Chiodini, 2015), and the -2‰ to -8‰ range of SCLM xenoliths(Cartigny, 2005), so may reflect a mantle source, but the range of values indicates either heterogeneities in the source carbon isotope ratios, or shallow modification. Fractionation affects the carbon isotope ratios of mantle-derived gases as they travel through the crust, interacting with rock, crustal fluids, and surface air. Additional contributions to CO_2 measured at the surface may also come from mixing, such as with biogenic CO_2, although this is likely to be a minor contribution at Erebus.

The measurements at Hut Cave (Fig 5) suggest that $\delta^{13}C$ is stable over short time periods (about 14 days) at both sites (Hut Cave main vent and Hut Cave Vent C), with no notable difference corresponding to sampling depth in the soil (Deep probe, Shallow probe).

We consider scenarios that could determine the range of carbon isotope ratios observed from a combination of source signatures and subsequent fractionation or other modification. We first rule out the possibility that the CO_2 originates from a heavy $\delta^{13}C$ end-member. A heavy end-member would need to reflect the original mantle signature and modification in the crust, prior to shallower processes causing fractionation, to lighter values. At Etna, a similarly heavy end-member is attributed to modification by crustal carbonate sediments (D'Alessandro et al., 1997; Correale et al., 2015). Such an influence is unlikely at Erebus, as there is limited evidence for carbonate basement rock in the crust beneath the McMurdo Sound area (Sims et al., 2008; Fielding et al., 2011; Scopelliti et al., 2011; Phillips et al., 2018), so we consider this improbable. It is more likely that the lighter values reflect an original mantle signature close to MORB values e.g. -4.5 ‰, Cartigny et al. (2001); -5 to -8 ‰, Javoy et al. (1986), or Subcontinental Mantle Lithosphere of around -3.5 ‰ (Bräuer et al., 2016; Lee et al., 2017) and modification is a result of shallow fractionation in the crust.

We also note that there is potential heterogeneity in the mantle source beneath the WARS. The compositions of Erebus lineage lavas indicate HIMU mixed with DMM type mantle, but their mantle source is considered to be heterogeneous (Sims et al., 2008). Correale et al. (2017) report WARS mantle $\delta^{13}C$ values of -2.5 to -4.5‰ in mantle xenoliths found in Northern Victoria Land. If similar values apply for the Erebus volcanic province mantle, then our measured carbon isotope ratios could be achieved with only minor fractionation.

However, we do not expect that heterogeneity in carbon isotope ratios at mantle depths could be preserved over very small spatial distances such that distinct $\delta^{13}C$ values were measured at sites only hundreds of metres apart. We therefore assume a lighter source $\delta^{13}C$. An initial $\delta^{13}C$ of -4‰, for example, could cover most of our range of measured values with about +3‰ fractionation. Fractionation processes, such as through magmatic degassing, hydrothermal dissolution, or transport through soil, are the next step in explaining how the measured range of compositions could have been generated.

Potential influences on the nature and extent of fractionation include (i) the depths and temperatures of shallow degassing magma bodies; (ii) diffusive and advective transport of CO_2; and (iii) the presence and temperatures of any hydrothermal systems, which may relate to the presence of magma bodies and water availability (Table 5). We next consider each of these factors, noting that mixing with non-volcanic CO_2 sources would require large quantities of CO_2 with distinct $\delta^{13}C$, and cannot be an important effect here. Although biological and surface air signatures are lighter than mantle, surface air only contributes about 400 ppm of CO_2, and with limited biological activity on Erebus, significant microbial CO_2 would be required to alter the isotope ratios of the projected 100% CO_2.

(i) Fluxing of CO_2 through the magmatic column is often invoked to explain high CO_2 emissions from Erebus lava lake (Oppenheimer et al., 2011), so the emissions we measure are likely to be sourced from depth, as well as from shallower phonolite magma bodies. Fractionation by magmatic degassing results in lighter carbon isotope ratios.

In such a scenario, emissions at Tramway and Sauna cave, and to a lesser extent Cathedral and Warren caves (extrapolated to – 3 to – 4.5‰ at 100% CO_2), would be fractionated to lighter end-members and derive from shallower sources. With a source $\delta^{13}C$ likely close to – 4‰, little fractionation would be required to explain our lightest values. The upper limit on fractionation by magmatic degassing for basalts is well above this, at around -4‰ (Gerlach and Taylor, 1990; Javoy et al., 1978; Mattey, 1991), though no published data are available for basanite, which is the parent melt at Erebus. While degassing pathways are too small to be resolved, Zandomeneghi et al. (2013) do identify larger potential magma bodies at Erebus using seismic tomography. Tramway and Sauna are associated with shallow high velocity zones, i.e. potential hot intrusions, while Hut Cave and Ice Tower Ridge overlie hydrothermal systems or chilled magma bodies. Sources beneath Warren and Cathedral are less clear. The hot intrusions could be a source of gas that has fractionated during magmatic degassing, but this does not account for the heavier $\delta^{13}C$ at other sites such as Periscope Cave or the crater rim. Another mechanism is required for fractionation to heavier values.

(ii) Federico et al. (2010) report significant transport-driven fractionation effects during diffuse degassing of CO_2 that can lead to apparent increases in $\delta^{13}C$. This is an important consideration, as there can be fractionation of over 4 ‰ in the interaction between CO_2 and air during diffusion into shallow soil layers(Camarda et al., 2007).

This is a difficult effect to evaluate, as many factors may contribute to transport-driven fractionation, including the soil type and CO_2 flux, the pump rate and depth of the sample probe, and wind. The latter is most likely to have affected measurements at Ice Tower Ridge and Tramway Ridge, as these were warm ground areas, exposed to the surface. However, they have very distinct isotope ratios: Tramway Ridge has the one of the lightest of any site (-4.99 ‰), whereas Ice Tower Ridge has a much heavier signature (-1.92 ‰), despite similar exposure to the wind, surface temperatures and sampling methods at both sites. At Hut Cave, sample probes inserted at different depths at the same vent next to one another, and at a second site where gas was blown rapidly out of a crack, yielded very similar $\delta^{13}C$ values after 1-2 days of pumping, suggesting there were no large kinetic effects at shallow depths for that site. We also observe similarities between $\delta^{13}C$ measured at different vents within other caves (e.g. Warren, Sauna), despite different rates of gas emission, differing amounts of soil, and different soil temperatures. This does not rule out the possibility of fractionation due to diffuse degassing, and by contrast we do see some variation in $\delta^{13}C$ at Periscope.

However, the overall consistency between vents within each sampling site suggests that factors other than kinetic fractionation have a greater role in determining $\delta^{13}C$.

(iii) The shallow plumbing at Erebus may be complex on small spatial scales, as evidenced by the variability of plume gas compositions from its lava lakes ((Oppenheimer and Kyle, 2008)) and changes to summit degassing sites over short time periods. Subsurface magmatic and hydrothermal features could be a factor in the spatial variability of carbon isotope ratios from flank sites. Dissolution of CO_2 in a shallow hydrothermal system and fractionation between dissolved, gaseous, and any precipitating phases (Mook et al., 1974) can cause fractionation. Dissolution in a low temperature hydrothermal system favours lighter values in the gas. This requires temperatures <120°C for HCO_3^-(aq) – CO_2 (g) equilibrium fractionation, or <192°C in the calcite – CO_2 (g) system (Bottinga, 1968; Zhang et al., 1995; Szaran, 1997; Myrttinen et al., 2012). By contrast, dissolution of a light CO_2 end-member in higher temperature systems (i.e. >120°C in equilibrium with aqueous HCO_3^-, or >192°C with calcite) could cause fractionation to heavier values.

Table 5. Properties of degassing sites potentially correlating with measured carbon isotope ratios

Site	**Seismic tomography[1]**	**Max vent temperatures[2]**	**Relative depth[3]**	**Projected $\delta^{13}C$ (‰)[4]**	**$[CO_2]$(%)[5]**
Tramway Ridge warm ground	LVZ	Hot (59°C)	Surface	-5 to -4	1.3-1.8
Ice Tower Ridge warm ground	HVZ	Hot (59.5°C)	Surface	-1	0.11-0.32
Sauna Cave	LVZ	Hot (43.5°C)	Deep	-4	0.63-1.3
Cathedral Cave	LVZ?	Cool (15°C)	Deep	-3.5	0.67-1.3
Warren Cave	HVZ?	Cool (15.5°C)	Deep	-3	0.7-1.6
Hut Cave	HVZ	Cool (9.7°C)	Shallow	-2	0.24-0.25
Periscope Cave	LVZ	Warm (21°C)	Surface	-2 to -1	0.22-0.34

[1]From Zandomeneghi et al. 2013. [2]Hottest vent temperatures at sample sites in this study. [3]Relative to local ground surface. Periscope cave is largely horizontal, while the vents in Hut Cave are below ground surface (approx. 2-4 m). Warren, Cathedral-Mammoth, and Sauna, all have entrances over 10 m below the surface ice. [4]See figure 3 for projected mixing lines. [5]Concentrations for Warren, Tramway, and Sauna are estimates; those for Cathedral were measured directly by Delta Ray before dilution. Hut, Periscope, and ITR concentrations could be measured directly during the Delta Ray analyses.

The highest outlet temperatures (59°C) were observed at both Tramway and ITR warm ground sites, which bracket the measured range of carbon isotope ratios. The difference between the two could be explained by the presence (ITR) or absence (Tramway) of a high temperature hydrothermal system. If we assume fractionation solely between dissolved bicarbonate – gaseous CO_2 and take Tramway to represent the unmodified magmatic and most mantle-like gas, fractionation factors suggest a temperature of about 200°C could give a +4‰ heavier $\delta^{13}C$-CO_2 (Myrttinen et al., 2012), accounting for maximum projected difference measured at ITR compared to Tramway. Lower temperature systems would experience less fractionation, explaining the intermediate values observed at Hut and Periscope caves. Carbon dioxide dissolves more readily into aqueous solutions at low temperatures (Lowenstern, 2001), so that lower fluxes are also expected above low temperature hydrothermal systems. This may account for small difference in fluxes between Tramway and ITR, and high CO_2 concentrations in bag samples at Tramway compared to ITR or the caves.

Samples from the crater rim also have a heavier $\delta^{13}C$ signature despite CO_2 concentrations being close to air. This could result from removal, through dissolution, of magmatic CO_2, combined with fractionation in a high temperature hydrothermal system similar to what we propose beneath ITR.

The source of hydrothermal water is likely meteoric, but the depth at which the interaction with magmatic gas begins is unknown. The water source is important in considering whether it is plausible that the CO_2 emissions at Periscope (-2 to -1 ‰) could be affected by hydrothermal interactions without any similar effects nearby at Tramway (-5 to -4 ‰). Localised melting is observed within caves, and refreezing results in the increased ice density measured by Curtis (2015). Periscope and Hut caves, where surface snow is frequently blown in to the caves, have heavier projected $\delta^{13}C$ (-2 to -1‰) than the deeper Sauna, Warren, and Cathedral caves. This might suggest that gases emitted from shallow caves are more influenced by shallow percolation of meltwater and isotopic fractionation due to dissolution, but only if meltwater could reach sufficiently high temperatures to cause fractionation to heavier $\delta^{13}C$. We do not have enough evidence to determine whether ice thickness or proximity to the base of the snowpack might influence degassing. In addition to melting in the summit area, if a larger subglacial groundwater system (Flowers, 2015) were to exist beneath the lower glaciated flanks of Erebus, there could be a more extensive hydrothermal system circulating to greater depths.

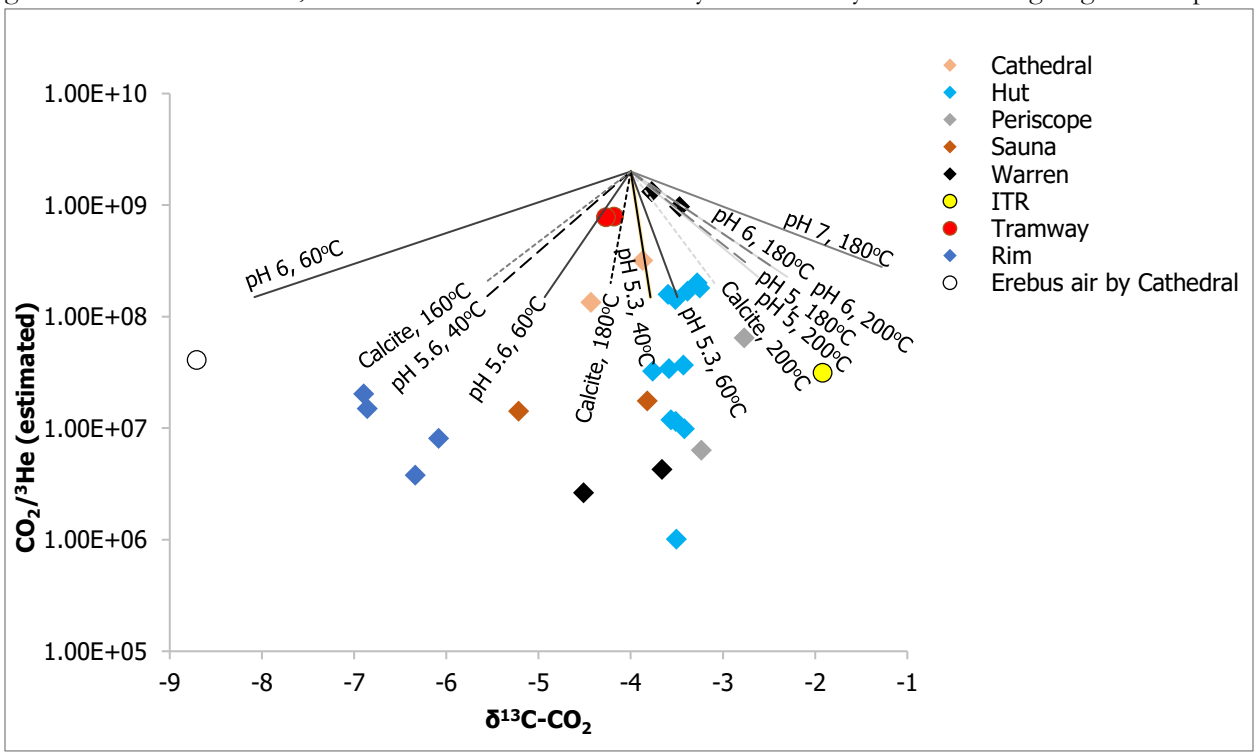

Figure 10. Possible fractionation pathways from partitioning of CO_2 (g) in water with precipitated calcite or aqueous HCO_3^- and H_2CO_3, which is pH dependent. $CO_2/^3He$ ratios are from GC-QMS measurements of CO_2 and total He, with ^3He estimated from a constant R/Ra, assumed to be 1.18, from IRMS analyses of 2012 copper tube samples. The fractionation lines start from an assumed $CO_2/^3He$ of $2x10^9$, which are likely values for DMM and MORB (Resing et al., 2004; Barry et al., 2014) as well as close to the lower values found by Barfod et al. (1999) for gases from the Cameroon volcanic line. They are calculated up to a dissolved CO_2 fraction of 93% or precipitated calcite of 90%.

For Rayleigh fractionation of CO_2 dissolving in water, with partitioning between CO_2 (g) and calcite or HCO_3^- (aq), using fractionation factors from the literature (Malinin et al., 1967; Clark and Fritz, 1997), we can

consider the range of concentrations and $\delta^{13}C$-CO_2 that could be generated by fractionation in a hydrothermal system. Using CO_2/He ratios from GC-QMS analyses, and assuming a constant R/Ra, of 1.18, which is the highest measured from our samples, we follow Gilfallan et al. (2009) to plot estimated $CO_2/^3He$ vs $\delta^{13}C$ (Fig 10). We see in Figure 10 that direction of fractionation is influenced both by temperature and pH, with fractionation to heavier carbon isotope ratios in the discharging CO_2 requiring high temperatures or lower pH. With calcite precipitation, still higher temperatures are required, as the crossover point when $\delta^{13}C$-CO_2 begins fractionating to heavier values is at around 192°C (Malinin et al., 1967). We consider the range of carbon isotope ratios that can be generated with slight variations in temperature or pH conditions to support hydrothermal fractionation at Erebus. The mechanism for CO_2 loss and the water pH would be required to constrain the temperature. Regardless of these, however, CO_2 loss of over 99% of the original gas is required to reach the measured amounts. The most likely scenario, therefore, is dilution and removal of CO_2, through air mixing combined with dissolution in a high temperature or slightly acidic hydrothermal system.

4.1.2 Oxygen isotope ratios

Attempts to calculate the original oxygen isotope ratios of any water in equilibrium with the measured CO_2, following Chiodini et al. (2000) are prevented by the lack of constraints on equilibration temperatures and H_2O/CO_2 ratios. Sample temperatures are relatively low, and equilibrium is likely to be with liquid water where it is present. The more dilute samples from the crater rim resemble air, which is consistent with the rapid kinetics of $\delta^{18}O$ equilibration between CO_2 and H_2O, whereas the lightest oxygen isotope ratios are at Tramway Ridge and ITR, where steaming ground indicates water emissions. We did not collect snow samples from the same sites for oxygen isotope data, but our warm ground data may be consistent with CO_2 re-equilibration to Erebus snowmelt with light $\delta^{18}O$ due to the altitude (Assonov et al., 2005). The cave samples and cave air fall in an intermediate region, likely indicating a combination of meltwater and air contamination, rather than a heavier magmatic water component. The higher temperature fumaroles in the main crater, and the concentrated plume closer to the lava lake, could not be accessed, but in theory could provide more reliable constraints on oxygen isotopes in combination with $\delta^{18}O$-H_2O from snow (e.g. Curtis, 2015).

4.1.3 CO_2 flux and concentration

Direct flux measurements at Side Crater, Ice Tower Ridge, and Tramway range from around 120 – 290 $g.m^{-2}.d^{-1}$ with a total of about 8.2 $t.d^{-1}$. This is lower than the flux estimated for total flank degassing by Wardell et al. (2003), who quantified fluxes out of openings on ice towers and caves as well as warm ground, and found higher fluxes overall, totalling 40 $t.d^{-1}$. Their method was based on fewer measurements over a greater area and it is likely that our measurements did not cover the same areas. We included Side Crater, which was not in their study, whereas they report higher fluxes on upper Tramway Ridge (4760 $g.m^{-2}.d^{-1}$), suggesting that our coverage of Tramway was different or that fluxes have changed. Soil degassing at the ITR site appears consistent between our measurements in 2015 and 2016, suggesting stability over these time periods. The CO_2 concentrations from GC-QMS analyses do not exceed 2.9%, which is consistent with amounts measured by Wardell et al. (2003).

If we assume that the difference in CO_2 fluxes between Tramway and ITR is due to a 200°C hydrothermal system beneath ITR dissolving CO_2 as bicarbonate, we can use the solubility of CO_2 in water to calculate that the approx. 44 $g.m^{-2}.d^{-1}$ that is lost must be interacting with a 6.5 x 10^6 L volume of water per day. Given our estimates of the surface area at ITR (9164 m^2), this could suggest an aquifer thickness of 2 – 14 m depending on capacities of 5 – 33% water for the aquifer.

Our attempts to quantify diffuse CO_2 flux in caves were complicated by high CO_2 content in the cave air, which often prevented accurate flushing of the accumulation chamber. In these cases, cave air CO_2 exceeded that measured in samples from the ground. Constant high gas flow may be responsible for more established deep caves at Warren and Cathedral.

Our flux measurements fall into two broad populations (Fig. 9), the reason for which is not clear. Hydrothermal dissolution of CO_2 cannot account for the CO_2 flux population distributions, as Tramway and ITR have similar distributions, although they have different overall fluxes and carbon isotope ratios that are consistently different. In addition, although CO_2 solubility in water decreases with temperature, ITR has similar or lower concentrations of CO_2 in the sampled gases compared to Hut and Periscope, despite a projected higher temperature hydrothermal system based on its heavier carbon isotope ratios. Combined with the observation that low CO_2 concentration samples have more air-like carbon isotope ratios, this makes it more likely that the degree of air contamination is responsible for the observed CO_2 flux distribution, i.e. lower fluxes could be associated with a higher proportion of atmosphere-derived air.

4.2 Gas compositions and atmospheric air

Most copper tube and Giggenbach bottle samples are dominated by air (Fig. 3, Table 1). This could be due to contamination during sampling, mixing with cave air before sample collection, recirculation of air through the volcanic edifice (e.g. Bergfeld et al., 2015), or incorporation of air into the convecting lava lake at the summit followed by transport from the degassing magma to the ice caves.

If gas flow out of vents is unsteady, pumped samples may contain cave air mixed with occasional pulses of more deeply-sourced gas, which could explain why copper tube sample compositions are variable. This variability may not be picked up over the area and timescales of the flux meter measurements or in collecting 1 L of sample for carbon isotope measurements. The nitrogen-rich samples could then represent either a magmatic end-member, or an air-contaminated CO_2 rich gas with oxygen removed (Fig. 3a). Airflow resonance in caves is a recognized phenomenon (Cigna, 1968) that may result in high frequency periodicities in CO_2 concentrations (Faimon et al., 2012). Such observations have focused on cave air and air at cave entrances, but we speculate that similar processes on a smaller scale may affect compositions between duplicate copper tubes at cave vents.

Air contributions to vent degassing could also result from more systematic incorporation of atmospheric air via caves or permeable volcanic rock and soil. Mechanisms for this could include differential air temperature or pressure, or wind -driven mixing. Barometric pumping occurs at Warren Cave, and seems to only affect the degree to which air is pulled out of ice towers and caves (Curtis and Kyle, 2011). However, there are other drivers of circulation that have been identified both in caves and on mountain slopes: the temperature-driven chimney effect, with cold air pulled in at lower entrances and warm air emitted at higher ones, and 'mountain breathing' caused by wind (Woodcock, 1987). These can occur in porous soils even in the absence of caves or volcanic degassing (Thorstenson et al., 1998; Bergfeld et al., 2015). At Erebus, fractures in the ice cover on the lower flanks, for example at glacial crevasses, and exposed rock or soil in the summit caldera, could permit atmospheric air into the edifice. Emissions of CO_2 in such instances could also be affected by atmospheric conditions and wind-driven circulation (Lewicki et al., 2007; Ogretim et al., 2013). The lava lake

is open to the atmosphere and is another potential site for mixing; however, entrainment of cold air at lower levels, rather than at the summit where hot gas is also emitted, is more consistent with the chimney effect.

The N_2/Ar and O_2/Ar ratios of gas samples tend to be within the ranges measured for air samples. The N_2/O_2 concentrations, however, range from air-like to having O_2 below detection. In N_2-Ar-O_2 space the N_2-O_2 and Ar-O_2 variations are linear, implying that the nitrogen-rich gas results from oxygen being removed without affecting the N_2/Ar ratios, rather than from magmatic gas containing excess nitrogen mixing with air (Fig 3c).

An additional mechanism for modifying air or magmatic gas is dissolution in hydrothermal waters, which is likely to have affected carbon isotope ratios through dissolution of CO_2. Similar fractionation can occur between gases. The solubility of CO_2 in neutral waters is much higher than that of Ar and O_2, which have similar solubilities, while N_2 is less soluble (Sander, 2015). We can calculate the ratios of these species in equilibrium with the exsolved gas at changing temperatures, assuming some initial ratios and temperatures (Fig 11).

The difference between measured gas ratios and those of the same species dissolved in pure water is at a maximum at 0°C. At higher temperatures, this difference decreases, so re-exsolution from cooling water could account, for example, for increasing CO_2/O_2 or decreasing N_2/Ar ratios (Fig 11). However, the measured range of ratios is far greater than the maximum fractionations indicated by these calculations. Despite the similarity in solubilities between Ar and O_2, the spread of N_2/O_2 is much greater than that of N_2/Ar and cannot be explained by gas dissolution and re-exsolution. In the following sections we show that oxygen removal, rather than a high nitrogen content, is also supported by $\delta^{15}N$ and argon isotope data.

This is also consistent with the relationship between CO_2 and N_2/Ar (Fig. 3b). An initial magmatic gas can be partially stripped of CO_2 in a hydrothermal system. Mixing a small fraction of this gas with air would not noticeably affect N_2/Ar, given that mantle, ASW, and air values for N_2/Ar are relatively close. Oxidation of the surrounding rock could lead to an oxygen depleted air-like composition, potentially retaining some CO_2 whose carbon isotope composition reflects hydrothermal interaction. Combustion at the lava lake surface would be a second mechanism to remove oxygen, where magmatic gas could mix with oxygen-depleted air from the surface. However, we suggest that the first scenario is more likely given that pulling such significant proportions of cold air into the lava lake is counter to the chimney effect. We speculate that there is a further possibility of interaction between air and magmatic gases at high temperatures (Martin et al., 2006) but at greater depths in the plumbing system, rather than at the lava lake. Oxidation by reaction between air and magmatic gas rather than rock could also remove CO and H_2 (Giggenbach, 1987), accounting for the low proportion of these species in our samples, though oxidation of CH_4 by oxygen will be slower (Li and Hoflund, 2003). Regardless of the mechanism for oxygen removal, the variability in oxygen content between samples collected in the same time periods also shows that air mixing occurs throughout the system. This could be due to unsteady supply of a magmatic-hydrothermal gas that has been stripped of oxygen, or to variations in the amount of air added subsequently.

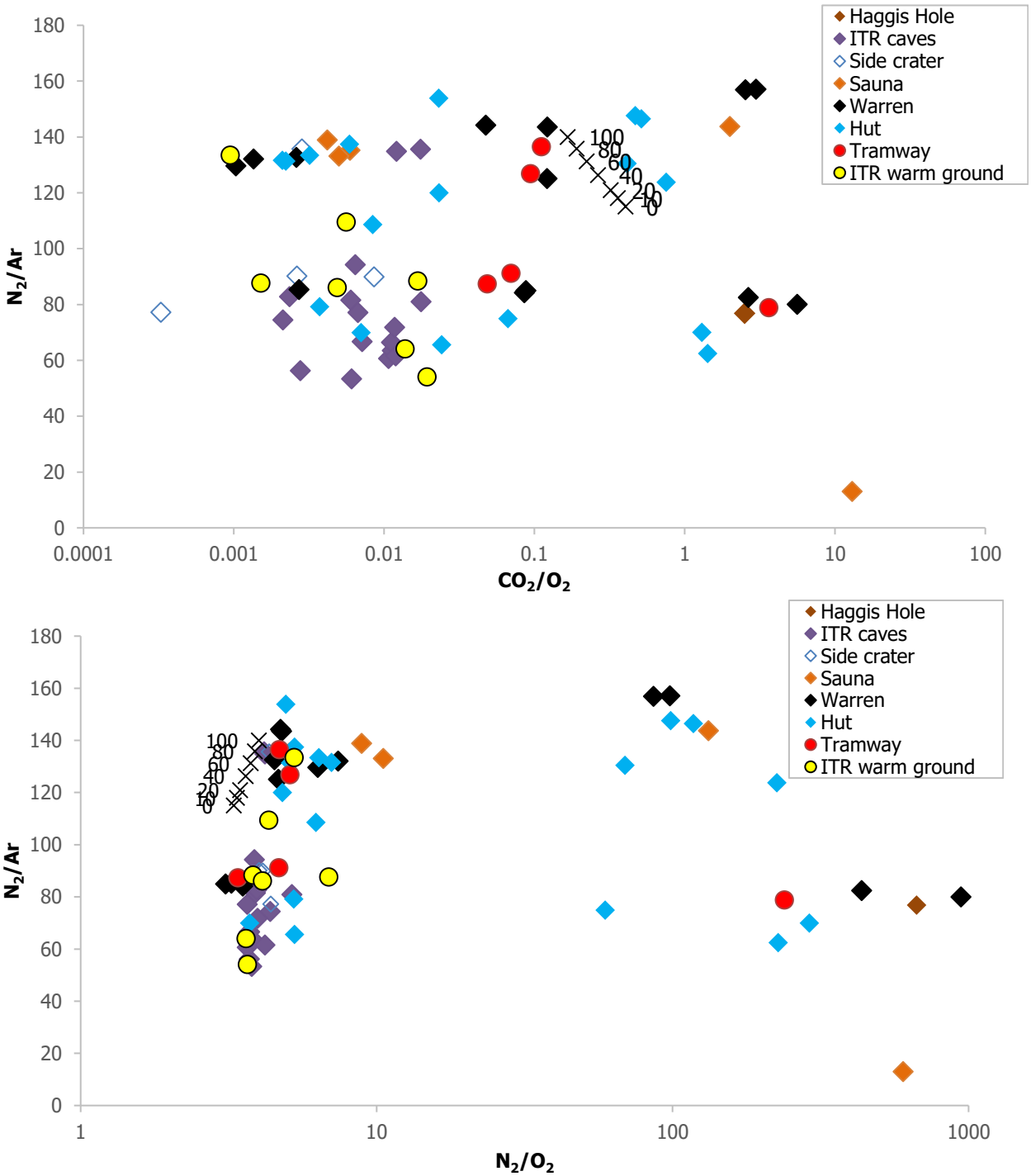

Fig 11. Examples of projected gas ratios from dissolution and re-exsolution of gas (N_2/Ar = 83, N_2/O_2 = 4, CO_2/O_2 = 1.7) in water cooling from 100 to 0°C (Henry's Law constants from Sander 2015). Labels indicate temperature of the water. from which degassing occurs. The range of these ratios produced in this way is smaller than observed in our gas samples, particularly compared to the spread of the x-axis.

4.3 Nitrogen and argon isotopes

Variations in $\delta^{15}N$ are small. Most samples are air-like, consistent with N_2/Ar ratios. A range of about -1.5 – 0.5‰ suggests a minor contribution from a MORB-type mantle component. Projecting a mixing line between air and the lightest samples towards $O_2/N_2 = 0$ gives a nitrogen isotope ratio of about -1.8‰, somewhat heavier than commonly cited MORB mantle values (Marty and Zimmermann, 1999; Mohapatra and Murty, 2004). We consider this to be the closest to source values, as kinetic fractionation during open system magmatic degassing is unlikely (Fischer et al., 2005) and would occur alongside fractionation of $\delta^{13}C\text{-}CO_2$ (Cartigny et al., 2001).

A three-component mixing model (Fig 12) can be used to examine the likely contributions from mantle, air or air-saturated water (ASW) at 0°C, and sediment sources, following Sano et al. (2001). The $N_2/^{36}Ar$ values here are derived from the average $^{40}Ar/^{36}Ar$ of 294.07 of our data. This shows that most of our data can be explained by mixing between a mantle end-member and air. As described by Sano et al. (2001), the mixing equations can be used to calculate the contributions of each end-member. Some samples (HUT1, ITR-UWG-11) resemble air despite being emitted at higher than ambient temperatures. The highest potential mantle contribution is from Sauna cave (Sauna-A-2) where 38 % (if mixed with air) to 57% (mixing with ASW) could be mantle-derived.

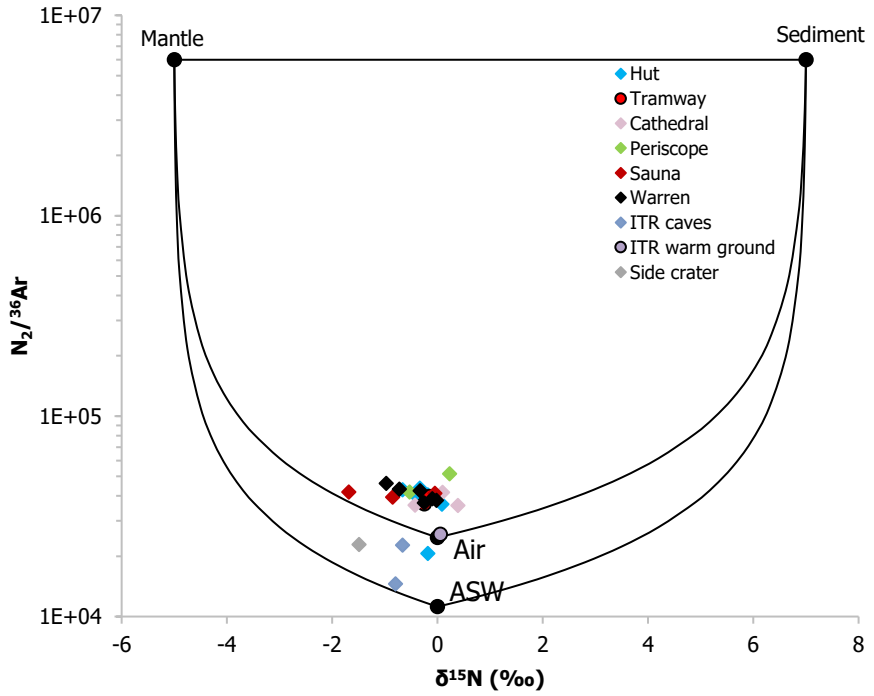

Figure 12. $N_2/^{36}Ar$ vs $\delta^{15}N$ using ^{36}Ar from argon content in each sample and average $^{40}Ar/^{36}Ar$ ratio of all samples analysed for argon isotopes (294.1), following Sano et al. (2001).

However, an alternative possibility to mixing is that fractionation of nitrogen between gas and dissolution in water is responsible for the variation in isotope ratios. Experiments by Lee et al. (2015) measured fractionations from +0.91‰ for N_2 dissolved in water at 5°C to -0.42‰ at 60°C, with a crossover at 40°C. Regardless of whether fractionation or mixing are responsible for the range of $\delta^{15}N$, the samples from Sauna Cave with the lightest nitrogen isotope values and highest temperatures are the least modified by atmospheric air contamination or dissolution and exsolution from the original magmatic gas.

Samples from sites other than Sauna Cave, even where N_2/O_2 ratios are high, have more air-like $\delta^{15}N$. This indicates that the process by which N_2/O_2 is increased is independent of the nitrogen source; oxygen is removed from gases that are predominantly air as well as from those that contain a greater mantle-derived component. Argon isotopes are also air-like, with one relatively argon-rich sample (HUT-shallow-14) having a slightly higher than air (295) $^{40}Ar/^{36}Ar$ of 331.

These stable isotope ratios indicate a primarily air-derived gas, which requires a mechanism for removal of oxygen rather than the addition of nitrogen. As discussed in the previous section, removal of O_2 by dissolution in water would similarly affect Ar and is inconsistent with observed trends shown in Figures 2 and 10. Another mechanism is a redox reaction with gas or rock that removes oxygen from air. Examples might be reactions with and removal of reduced gas species such as CO, H_2, H_2S, and CH_4. Of these species, reaction of hydrogen sulfide with iron in rocks may account for sulfur species not being detected in flank degassing (Symonds et al., 2001). The remaining species are only observed in trace amounts in our samples. A more likely scenario is reaction of O_2 with rock close to the surface, resulting in oxidation of the rock and removal of O_2. A final possibility is that microbial oxidation sometimes exceeds the supply of oxygen from atmospheric air. At Warren and neighbouring caves, biological studies have found CO oxidizing bacteria (Tebo et al., 2015), but this cannot account for gas compositions that seem only to have oxygen removed, without increased CO_2. Some combination of these processes may be responsible for oxygen depleted gases.

4.4 Degassing model and implications

Figure 13 shows likely pathways contributing to the upper flank degassing of Erebus, with mixing between magmatic and atmospheric gas within the volcano, and interaction between gas and meltwater causing fractionation of elemental gas and carbon and nitrogen isotope ratios. It is likely that melting within void spaces extends from FIC scales to much smaller soil pore scales, with widespread basal melting wherever heat is sufficient. We cannot rule out the possibility that hydrothermal water could be sourced from a larger region extending beneath Erebus' glaciated lower flanks. The presence of a hydrothermal system suggests that previous phreatomagmatic activity may not be solely due to snow cover as previously assumed. Such a system has the potential to dissolve a small proportion of the CO_2 that would otherwise be degassing. While the carbon isotope ratios we measure can be attributed to dissolution of CO_2, the proportions of CO_2 we measured would require a much higher proportion be dissolved. The small difference in CO_2 flux at sites expected to be affected or unaffected by hydrothermal dissolution (about 2 $t \cdot d^{-1}$ between ITR and Tramway) and the composition of the measured gases indicates that dilution by air is more likely to be responsible for the relatively low proportion of CO_2 (< 3%).

While degassing from the Erebus summit crater has a partially shallow degassing signature affected by processes occurring within or just below the lake (Oppenheimer et al., 2009; Iacovino, 2015; Ilanko et al., 2015), upper flank degassing should be unaffected by conduit magma flow. Thus, gas measurements taken over time at warm ground or FIC may give some indication as to changes occurring within the shallow magma storage region, or to deeper sources of degassing. Our measurements show variations in small volume copper tube samples that may be due to temporal changes over short time scales. High resolution time series measurements in the field, of both composition and carbon isotope ratios, could be advantageous to understand high frequency variations. Field gas analyses for carbon isotope ratios are possible (Di Martino et al., 2016), but the power requirements and stable conditions currently required for analyses in the field pose a particular challenge on Erebus.

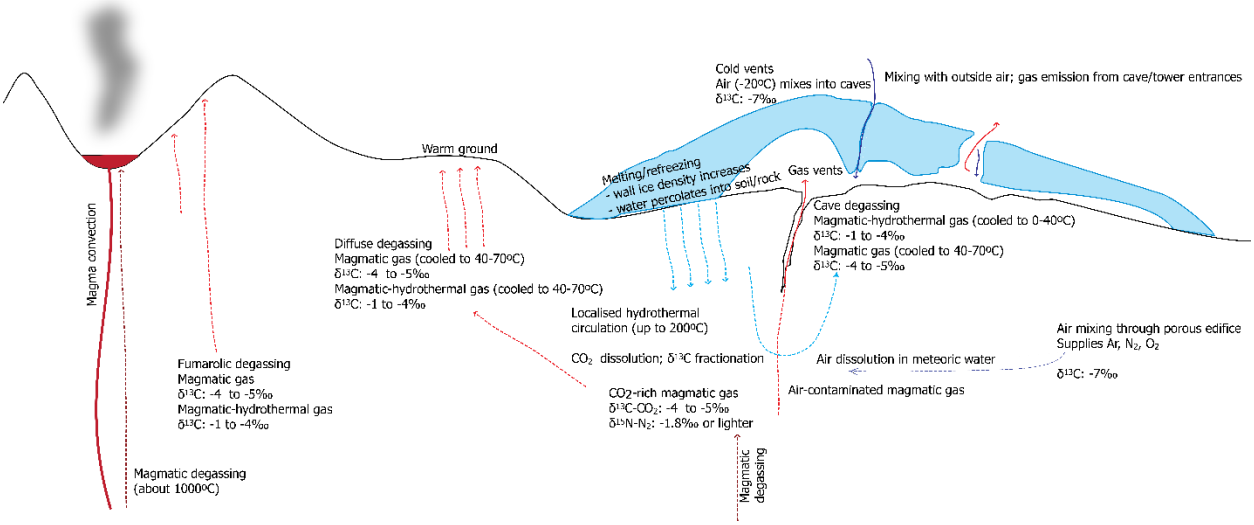

Figure 13. Schematic of upper flank degassing on Erebus. The original magmatic signature is modified by air contamination, and in some cases by interaction with a shallow hydrothermal system.

5. Conclusions

Despite contributing a relatively small proportion of the gas emitted from Erebus, low temperature degassing sites reveal information about the shallow interactions between magmatic gas, meltwater, and atmospheric air in the shallow volcanic edifice. The loss of CO_2 to the hydrothermal system has been estimated and its effects are seen in carbon isotope ratios of CO_2. Magmatic values are around -4‰, with fractionation to heavier values related to dissolution in water. Melting is observed in the warm cave environments and may contribute meteoric water to hydrothermal systems. Water availability varies locally, with potential shallow systems represented by high velocity structures such as that beneath Ice Tower Ridge (Zandomeneghi et al., 2013). While the pre-existing dyke intrusion provides pathways for magmatic gas ascent, there is also a greater degree of interaction with water at high temperatures, resulting in lower fluxes of CO_2, of about two-thirds of that at Tramway Ridge, and fractionation towards heavier carbon isotope ratios closer to -1‰, as the carbon isotopes equilibrate between gaseous CO_2 and other aqueous or precipitating phases, especially HCO_3^-, and possibly calcite. By contrast, shallow magma bodies at Sauna and Tramway suggested by low seismic velocity regions (Zandomeneghi et al., 2013) are associated with higher CO_2 fluxes and carbon isotope ratios less affected by shallow water or air interaction.

Samples at many sites contain a high proportion of air, showing that in addition to removal by dissolution, initial concentrations of CO_2 are diluted by air. Although this dilution may be shallow and localized, oxygen depleted samples also contain air-derived nitrogen, indicating that further modification causing oxygen removal must have occurred after air contamination. This suggests that atmospheric air mixes with the magmatic gas more systematically, possibly from wind-driven mountain breathing through the volcanic edifice. Nitrogen isotope ratios show that most samples are heavily influenced by air contamination. Oxygen-poor samples could then result from the removal of air-derived oxygen, though the exact mechanism, for example redox reactions with rocks, or microbial processes, remains unknown.

The identification and characterization of a liquid-dominated hydrothermal system at Erebus has important implications for availability of liquid water in the subsurface, and the potential for phreatomagmatic eruptions. A warm liquid water phase also provides an additional and previously unrecognized habitat for microorganisms living below the ice and permafrost region of the volcanic edifice.

Acknowledgements

This material is based upon work supported by the National Science Foundation through the Office of Polar Programs under grants 1443633 (to TF) and 1142083 (to PRK), and through the Division of Earth Sciences under grant 1664246 (to TF). We are grateful to Viorel Atudorei and the Centre for Stable Isotopes at UNM for assistance with laboratory analyses.

References

ASPA No. 175 management plan, 2014. Management Plan for Antarctic Specially Protected Area No. 175. High Altitude Geothermal Sites of the Ross Sea Region (including parts of the summits of Mount Erebus, Ross Island and Mount Melbourne and Mount Rittmann, northern Victoria Land), in: ATCM XXXVII Final Report. Presented at the Antarctic Treaty Consultative Meeting, Brasilia, pp. 199-225. https://www.ats.aq/documents/recatt/att553_e.pdf.

Assonov, S.S., Brenninkmeijer, C.A.M., Jöckel, P., 2005. The 18O isotope exchange rate between firn air CO2 and the firn matrix at three Antarctic sites. J. Geophys. Res. Atmospheres 110, D18310. https://doi.org/10.1029/2005JD005769

Barfod, D.N., Ballentine, C.J., Halliday, A.N., Fitton, J.G., 1999. Noble gases in the Cameroon line and the He, Ne, and Ar isotopic compositions of high μ (HIMU) mantle. J. Geophys. Res. Solid Earth 104, 29509–29527. https://doi.org/10.1029/1999JB900280

Barry, P.H., Hilton, D.R., Füri, E., Halldórsson, S.A., Grönvold, K., 2014. Carbon isotope and abundance systematics of Icelandic geothermal gases, fluids and subglacial basalts with implications for mantle plume-related CO_2 fluxes. Geochim. Cosmochim. Acta 134, 74–99. https://doi.org/10.1016/j.gca.2014.02.038

Behrendt, J.C., 1999. Crustal and lithospheric structure of the West Antarctic Rift System from geophysical investigations - a review. Glob. Planet. Change 23, 25–44. https://doi.org/10.1016/S0921-8181(99)00049-1

Behrendt, J.C., LeMasurier, W.E., Cooper, A.K., Tessensohn, F., Tréhu, A., Damaske, D., 1991. Geophysical studies of the West Antarctic Rift System. Tectonics 10, 1257–1273. https://doi.org/10.1029/91TC00868

Bergfeld, D., Evans, W.C., Howle, J.F., Hunt, A.G., 2015. Magmatic gas emissions at Holocene volcanic features near Mono Lake, California, and their relation ot regional magmatism. J. Volcanol. Geotherm. Res. 292, 70–83.

Bottinga, Y., 1968. Calculated fractionation factors for carbon and hydrogen isotope exchange in the system carbon dioxide-graphite-methane-hydrogen-water vapor. Geochim. Cosmochim. Acta 33, 49–64.

Bräuer, K., Geissler, W.H., Kämpf, H., Niedermannn, S., Rman, N., 2016. Helium and carbon isotope signatures of gas exhalations in the westernmost part of the Pannonian Basin (SE Austria/NE Slovenia): Evidence for active lithospheric mantle degassing. Chem. Geol. 422, 60–70. https://doi.org/10.1016/j.chemgeo.2015.12.016

Camarda, M., De Gregorio, S., Favara, R., Gurrieri, S., 2007. Evaluation of carbon isotope fractionation of soil CO_2 under an advective–diffusive regimen: A tool for computing the isotopic composition of unfractionated deep source. Geochim. Cosmochim. Acta 71, 3016–3027. https://doi.org/10.1016/j.gca.2007.04.002

Cartigny, P., 2005. Stable Isotopes and the Origin of Diamond. Elements 1, 79–84. https://doi.org/10.2113/gselements.1.2.79

Cartigny, P., Jendrzejewski, N., Pineau, F., Petit, E., Javoy, M., 2001. Volatile (C, N, Ar) variability in MORB and the respective roles of mantle source heterogeneity and degassing: the gase of the Southwest Indian Ridge. Earth Planet. Sci. Lett. 194, 241–257.

Chiodini, G., Allard, P., Caliro, S., Parello, F., 2000. 18O exchange between steam and carbon dioxide in volcanic and hydrothermal gases: implications for the source of water. Geochim. Cosmochim. Acta 64, 2479–2488. https://doi.org/10.1016/S0016-7037(99)00445-7

Chiodini, G., Cioni, R., Guidi, M., Raco, B., Marini, L., 1998. Soil CO_2 flux measurements in volcanic and geothermal areas. Appl. Geochem. 13, 543–552. https://doi.org/10.1016/S0883-2927(97)00076-0

Christoffersen, P., Bougamont, M., Carter, S.P., Fricker, H.A., Tulaczyk, S., 2014. Significant groundwater contribution to Antarctic ice streams hydrologic budget. Geophys. Res. Lett. 41, 2003–2010. https://doi.org/10.1002/2014GL059250

Cigna, A.A., 1968. An analytical study of air circulation in caves. Int. J. Speleol. 3, 41–54. https://doi.org/10.5038/1827-806X.3.1.3

Clark, I.D., Fritz, P., 1997. Environmental Isotopes in Hydrogeology. CRC Press, Boca Raton, FL.

Correale, A., Paonita, A., Rizzo, A.L., Grassa, F., Martelli, M., 2015. The carbon-isotope signature of ultramafic xenoliths from the Hyblean Plateau (southeast Sicily, Italy): Evidence of mantle heterogeneity. Geochem. Geophys. Geosystems 16, 600–611. https://doi.org/10.1002/2014GC005656

Correale, A., Pelorosso, B., Rizzo, A.L., Coltorti, M., Italiano, F., Bonadiman, C., 2017. A geochemical study of lithospheric mantle beneath Northern Victoria Land (Antarctica): main evidences from volatile content in ultramafic xenoliths, in: Geophysical Research Abstracts. Presented at the EGU General Assembly, European Geosciences Union, Vienna, pp. EGU2017-17484.

Curtis, A., 2015. Dynamics and global relevance of fumarolic ice caves on Erebus Volcano, Antarctica (Ph.D). New Mexico Institute of Mining and Technology, Socorro.

Curtis, A., Kyle, P.R., 2017. Methods for mapping and monitoring global glaciovolcanism. J. Volcanol. Geotherm. Res. 333–334, 134–144. https://doi.org/10.1016/j.jvolgeores.2017.01.017

Curtis, A., Kyle, P.R., 2011. Geothermal point sources identified in a fumarolic ice cave on Erebus volcano, Antarctica using fiber optic distributed temperature sensing. Geophys. Res. Lett. 38. https://doi.org/10.1029/2011GL0482

Curtis, A., Kyle, P.R., 2010. Erebus caves database. https://doi.org/10.15784/600381

D'Alessandro, W., Giammanco, S., Parello, F., 1997. CO_2output and d13C(CO_2) from Mount Etna as indicators of degassing of shallow asthenosphere. Bull. Volcanol. 58, 455–458.

de Moor, J.M., Fischer, T.P., Sharp, Z.D., Hilton, D.R., Barry, P.H., Mangasini, F., Ramirez, C., 2013. Gas chemistry and nitrogen isotope compositions of cold mantle gases from Rungwe Volcanic Province, southern Tanzania. Chem. Geol., Frontiers in Gas Geochemistry 339, 30–42. https://doi.org/10.1016/j.chemgeo.2012.08.004

Di Martino, M.R., Capasso, G., Camarda, M., 2016. Spatial domain analysis of carbon dioxide from soils on Vulcano Island: implications for CO_2 ouput evaluation. Chem. Geol. 444, 59–70. https://doi.org/10.1016/j.chemgeo.2016.09.037

Dibble, R.R., Kyle, P.R., Skov, M.J., 1994. Volcanic activity and seismicity of Mount Erebus, 1986-1994. Antarct. J. U. S. 29, 11–14.

Faimon, J., Troppova, D., Baldik, V., Novotny, R., 2012. Air circulation and its impact on microclimatic variables in the Cısarska Cave (Moravian Karst, Czech Republic). Int. J. Climatol. 32, 599–623. https://doi.org/10.1002/joc.2298

Federico, C., Corso, P.P., Fiordilino, E., Cardellini, C., Chiodini, G., Parello, F., Pisciotta, A., 2010. CO_2degassing at La Solfatara volcano (Phlegrean Fields): Processes affecting $\delta^{13}C$ and $\delta^{18}O$ of soil CO_2. Geochim. Cosmochim. Acta 74, 3521–3538. https://doi.org/10.1016/j.gca.2010.03.010

Fielding, C.R., Browne, G.H., Field, B., Florindo, F., Harwood, D.M., Krissek, L.A., Levy, R.H., Panter, K.S., Passchier, S., Pekar, S.F., 2011. Sequence stratigraphy of the ANDRILL AND-2A drillcore, Antarctica: A long-term, ice-proximal record of Early to Mid-Miocene climate, sea-level and glacial dynamism. Palaeogeogr. Palaeoclimatol. Palaeoecol. 305, 337–351. https://doi.org/10.1016/j.palaeo.2011.03.026

Fischer, Takahata, N., Sano, Y., Sumino, H., Hilton, D.R., 2005. Nitrogen isotopes of the mantle: insights from mineral separates. Geophys. Res. Lett. 32, L11305. https://doi.org/10.1029/2005GL022792

Fischer, T.P., Chiodini, G., 2015. Volcanic, Magmatic and Hydrothermal Gases, in: Sigurdsson, H., Houghton, B., McNutt, S., Rymer, H., Stix, J. (Eds.), The Encyclopedia of Volcanoes. pp. 779–797.

Fischer, T.P., Lopez, T.M., 2016. First airborne samples of a volcanic plume for $\delta^{13}C$ of CO_2 determinations. Geophys. Res. Lett. 43, 2016GL068499. https://doi.org/10.1002/2016GL068499

Flowers, G.E., 2015. Modelling water flow under glaciers and ice sheets. Proc. R. Soc. Math. Phys. Eng. Sci. 471, 20140907–20140907. https://doi.org/10.1098/rspa.2014.0907

Gerlach, T.M., Taylor, B.E., 1990. Carbon isotope constraints on degassing of carbon dioxide from Kilauea Volcano. Geochim. Cosmochim. Acta 54, 2051–2058. https://doi.org/10.1016/0016-7037(90)90270-U

Giggenbach, W.F., 1987. Redox processes governing the chemistry of fumarolic gas discharges from White Island. Appl. Geochem. 2, 143–161.

Giggenbach, W.F., 1975. A simple method for the collection and analysis of volcanic gas samples. Bull. Volcanol. 39, 132–145. https://doi.org/10.1007/BF02596953

Hall, J., Wilson, T., Henrys, S., 2007. Structure of the central Terror Rift, western Ross Sea, Antarctica. AK Cooper CR Raymond Al Eds Antarct. Keyst. Chang. World - Online Proc. 10th ISAES, USGS Open-File Report 2007-1047 5. https://doi.org/10.3133/of2007-1047.srp108

Harpel, C.J., Kyle, P.R., Dunbar, N.W., 2008. Englacial tephrostratigraphy of Erebus volcano, Antarctica. J. Volcanol. Geotherm. Res. 177, 549–568. https://doi.org/10.1016/j.jvolgeores.2008.06.001

Harry, D.L., Anoka, J.L., Jha, S., 2018. Geodynamic models of the West Antarctic Rift System: Implications for the mantle thermal state. Geosphere 14, 2407–2429. https://doi.org/10.1130/GES01594.1

Henrys, S., Wilson, T., Whittaker, J.M., Fielding, C., Hall, J., Naish, T., 2007. Tectonic history of mid-Miocene to present southern Victoria Land Basin, inferred from seismic stratigraphy in McMurdo Sound, Antarctica. AK Cooper CR Raymond Al Eds Antarct. Keyst. Chang. World - Online Proc. 10th ISAES, Open-File Report USGS Open-Fie Report 2007-1047, 4. https://doi.org/10.3133/of2007-1047.srp049

Huybers, P., Langmuir, C., 2009. Feedback between deglaciation, volcanism, and atmospheric CO_2. Earth Planet. Sci. Lett. 286, 479–491. https://doi.org/10.1016/j.epsl.2009.07.014

Iacovino, K., 2015. Linking subsurface to surface degassing at active volcanoes: A thermodynamic model with applications to Erebus volcano. Earth Planet. Sci. Lett. 431, 59–74. https://doi.org/10.1016/j.epsl.2015.09.016

Ilanko, T., Oppenheimer, C., Burgisser, A., Kyle, P.R., 2015. Cyclic degassing of Erebus volcano, Antarctica. Bull. Volcanol. 77. https://doi.org/10.1007/s00445-015-0941-z

Iverson, N.A., Kyle, P.R., Dunbar, N.W., McIntosh, W.C., Pearce, N.J.G., 2014. Eruptive history and magmatic stability of Erebus volcano, Antarctica: insights from englacial tephra. Geochem. Geophys. Geosystems 15, 4180–4202. https://doi.org/10.1002/2014GC005435

Iverson, N.A., Lieb-Lappen, R., Dunbar, N.W., Obbard, R., Kim, E., Golden, E., 2017. The first physical evidence of subglacial volcanism under the West Antarctic Ice Sheet. Sci. Rep. 7, 11457. https://doi.org/10.1038/s41598-017-11515-3

Javoy, M., Pineau, F., Delorme, H., 1986. Carbon and nitrogen isotopes in the mantle. Chem. Geol., Isotopes in Geology—Picciotto Volume 57, 41–62. https://doi.org/10.1016/0009-2541(86)90093-8

Javoy, M., Pineau, F., Iiyama, I., 1978. Experimental determination of the isotopic fractionation between gaseous CO_2 and carbon dissolved in tholeiitic magma. Contrib. Mineral. Petrol. 67, 35–39.
Kyle, P.R., Moore, J.A., Thirwall, M.F., 1992. Petrologic Evolution of Anorthoclase Phonolite Lavas at Mount Erebus, Ross Island, Antarctica. J. Petrol. 33, 849–875. https://doi.org/10.1093/petrology/33.4.849
Lee, H., Fischer, T.P., de Moor, J.M., Sharp, Z.D., Takahata, N., Sano, Y., 2017. Nitrogen recycling at the Costa Rican subduction zone: The role of incoming plate structure. Sci. Rep. 7, 13933. https://doi.org/10.1038/s41598-017-14287-y
Lee, H., Muirhead, J.D., Fischer, T.P., Ebinger, C.J., Kattenhorn, S.A., Sharp, Z.D., Kianji, G., 2016. Massive and prolonged deep carbon emissions associated with continental rifting. Nat. Geosci. 9, 145–149. https://doi.org/10.1038/ngeo2622
Lee, H., Sharp, Z.D., Fischer, Tobias P., 2015. Kinetic nitrogen isotope fractionation between air and dissolved N_2 in water: Implications for hydrothermal systems. Geochem. J. 49, 571–573. https://doi.org/10.2343/geochemj.2.0380
LeMasurier, W.E., 2008. Neogene extension and basin deepening in the West Antarctic rift inferred from comparisons with the East African rift and other analogs. Geology 36, 247–250. https://doi.org/10.1130/G24363A.1
LeMasurier, W.E., 1990. Late Cenozoic volcanism on the Antarctic Plate: An overview, in: LeMasurier, W.E., Thomson, J.W., Baker, P.E., Kyle, P.R., Rowley, P.D., Smellie, J.L., Verwoerd, W.J. (Eds.), Antarctic Research Series. American Geophysical Union, Washington, D. C., pp. 1–17. https://doi.org/10.1029/AR048p0001
Lewicki, J.L., Hilley, G.E., Tosha, T., Aoyagi, R., Yamamoto, K., Benson, S.M., 2007. Dynamic coupling of volcanic CO_2 flow and wind at the Horseshoe Lake tree kill, Mammoth Mountain, California. Geophys. Res. Lett. 34. https://doi.org/10.1029/2006GL028848
Li, Z., Hoflund, G.B., 2003. A review on complete oxidation of methane at low temperatures. J. Nat. Gas Chem. 12, 154–160.
Lough, A.C., Wiens, D.A., Barcheck, C.G., Anandakrishnan, S., Aster, R.C., Blankenship, D.D., Huerta, A.D., Nyblade, A., Young, D.A., Wilson, T.J., 2013. Seismic detection of an active subglacial magmatic complex in Marie Byrd Land, Antarctica. Nat. Geosci. 6, 1031–1035. https://doi.org/doi:10.1038/ngeo1992
Lowenstern, J.B., 2001. Carbon dioxide in magmas and implications for hydrothermal systems. Miner. Deposita 36, 490–502. https://doi.org/10.1007/s001260100185
Lyon, G.L., Giggenbach, W.F., 1974. Geothermal activity in Victoria Land, Antarctica. N. Z. J. Geol. Geophys. 17, 511–521. https://doi.org/10.1080/00288306.1973.10421578
Malinin, S.D., Kropotova, O.I., Grinenko, V.A., Vernadskiy, V.I., 1967. Experimental determination of equilibrium constants for carbon isotope exchange in the system CO_2 (g)-HCO_3 (sol) under hydrothermal conditions. Geochem. Int. 4, 764–771.
Martin, A.P., Cooper, A.F., Price, R.C., 2014. Increased mantle heat flow with on-going rifting of the West Antarctic rift system inferred from characterisation of plagioclase peridotite in the shallow Antarctic mantle. Lithos 190–191, 173–190. https://doi.org/10.1016/j.lithos.2013.12.012
Martin, R.S., Mather, T.A., Pyle, D.M., 2006. High-temperature mixtures of magmatic and atmospheric gases. Geochem. Geophys. Geosystems 7. https://doi.org/10.1029/2005GC001186
Marty, B., Zimmermann, L., 1999. Volatiles (He, C, N, Ar) in mid-ocean ridge basalts: Assesment of shallow-level fractionation and characterization of source composition. Geochim. Cosmochim. Acta 63, 3619–3633.
Mattey, D.P., 1991. Carbon dioxide solubility and carbon isotope fractionation in basaltic melt. Geochim. Cosmochim. Acta 55, 3467–3473. https://doi.org/10.1016/0016-7037(91)90508-3
Mikucki, J.A., Auken, E., Tulaczyk, S., Virginia, R.A., Schamper, C., Sorenson, K.I., Doran, P.T., Dugan, H., Foley, N., 2015. Deep groundwater and potential subsurface habitats beneath an Antarctic dry valley. Nat. Commun. 6, 6831. https://doi.org/10.1038/ncomms7831

Mohapatra, R.K., Murty, S.V.S., 2004. Nitrogen isotopic composition of the MORB mantle: A reevaluation. Geochem. Geophys. Geosystems 5, Q01001. https://doi.org/10.1029/2003GC000612

Mook, W.G., Bommerson, J.C., Staverman, W.H., 1974. Carbon isotope fractionation between dissolved bicarbonate and gaseous carbon dioxide. Earth Planet. Sci. Lett. 22, 169–176. https://doi.org/10.1016/0012-821X(74)90078-8

Myrttinen, A., Becker, V., Barth, J.A.C., 2012. A review of methods used for equilibrium isotope fractionation investigations between dissolved inorganic carbon and CO_2. Earth-Sci. Rev. 115, 192–199. https://doi.org/10.1016/j.earscirev.2012.08.004

Ogretim, E., Crandall, D., Gray, D.D., Bromhal, G.S., 2013. Effects of atmospheric dynamics on CO₂ seepage at Mammoth Mountain, California, USA. J. Comput. Multiph. Flows 5, 283–294.

Oppenheimer, C., Kyle, P.R., 2008. Probing the magma plumbing of Erebus volcano, Antarctica, by open-path FTIR spectroscopy of gas emissions. J. Volcanol. Geotherm. Res. 177, 743–754. https://doi.org/10.1016/j.jvolgeores.2007.08.022

Oppenheimer, C., Lomakina, A.S., Kyle, P.R., Kingsbury, N.G., Boichu, M., 2009. Pulsatory magma supply to a phonolite lava lake. Earth Planet. Sci. Lett. 284, 392–398. https://doi.org/10.1016/j.epsl.2009.04.043

Oppenheimer, C., Moretti, R., Kyle, P.R., Eschenbacher, A., Lowenstern, J.B., Hervig, R.L., Dunbar, N.W., 2011. Mantle to surface degassing of alkalic magmas at Erebus volcano, Antarctica. Earth Planet. Sci. Lett. 306, 261–271. https://doi.org/10.1016/j.epsl.2011.04.005

Panter, K.S., Castillo, P., Krans, S., Deering, C., McIntosh, W., Valley, J.W., Kitajima, K., Kyle, P., Hart, S., Blusztajn, J., 2018. Melt Origin across a Rifted Continental Margin: a Case for Subduction-related Metasomatic Agents in the Lithospheric Source of Alkaline Basalt, NW Ross Sea, Antarctica. J. Petrol. 59, 517–558. https://doi.org/10.1093/petrology/egy036

Panter, K.S., Winter, B., 2008. Geology of the Side Crater of the Erebus volcano, Antarctica. J. Volcanol. Geotherm. Res., Volcanology of Erebus volcano, Antarctica 177, 578–588.

Phillips, E.H., Sims, K.W.W., Blichert-Toft, J., Aster, R.C., Gaetani, G.A., Kyle, P.R., Wallace, P.J., Rasmussen, D.J., 2018. The nature and evolution of mantle upwelling at Ross Island, Antarctica, with implications for the source of HIMU lavas. Earth Planet. Sci. Lett. 498, 38–53. https://doi.org/10.1016/j.epsl.2018.05.049

Rasmussen, D.J., Kyle, P.R., Wallace, P.J., Sims, K.W.W., Gaetani, G.A., Phillips, E.H., 2017. Understanding Degassing and Transport of CO_2-rich Alkalic Magmas at Ross Island, Antarctica using Olivine-Hosted Melt Inclusions. J. Petrol. 58, 841–861. https://doi.org/10.1093/petrology/egx036

Resing, J.A., Lupton, J.E., Feely, R.A., Lilley, M.D., 2004. CO_2 and ^3He in hydrothermal plumes: implications for mid-ocean ridge CO_2 flux. Earth Planet. Sci. Lett. 226, 449–464. https://doi.org/10.1016/j.epsl.2004.07.028

Rilling, S., Mukasa, S., Wilson, T., Lawver, L., Hall, C., 2009. New determinations of 40Ar/39Ar isotopic ages and flow volumes for Cenozoic volcanism in the Terror Rift, Ross Sea, Antarctica - Rilling - 2009 - Journal of Geophysical Research: Solid Earth - Wiley Online Library. J. Geophys. Res. 114. https://doi.org/10.1029/2009JB006303

Rocchi, S., Armienti, P., D'Orazio, M., Tonarini, S., Wijbrans, J.R., Vincenzo, G.D., 2002. Cenozoic magmatism in the western Ross Embayment: Role of mantle plume versus plate dynamics in the development of the West Antarctic Rift System. J. Geophys. Res. Solid Earth 107, ECV 5-1-ECV 5-22. https://doi.org/10.1029/2001JB000515

Rothman, L.S., Gordon, I.E., Babikov, Y., Barbe, A., Chris Benner, D., Bernath, P.F., Birk, M., Bizzocchi, L., Boudon, V., Brown, L.R., Campargue, A., Chance, K., Cohen, E.A., Coudert, L.H., Devi, V.M., Drouin, B.J., Fayt, A., Flaud, J.-M., Gamache, R.R., Harrison, J.J., Hartmann, J.M., Hill, C., Hodges, J.T., Jacquemart, D., Jolly, A., Lamouroux, J., Le Roy, R.J., Li, G., Long, D.A., Lyulin, O.M., Mackie, C.J., Massie, S.T., Mikhailenko, S.N., Müller, H.S.P., Naumenko,

O.V., Nikitin, A.V., Orphal, J., Perevalov, V.I., Perrin, A., Polovtseva, E.R., Richard, C., Smith, M.A.H., Starikova, E., Sung, K., Tashkun, S.A., Tennyson, J., Toon, G.C., Tyuterev, V.G., Wagner, G., 2013. The HITRAN2012 molecular spectroscopic database. J. Quant. Spectrosc. Radiat. Transf. 130, 4–50.

Sander, R., 2015. Compilation of Henry's law constants (version 4.0) for water as solvent. Atmospheric Chem. Phys. 15, 4399–4981. https://doi.org/10.5194/acp-15-4399-2015

Sano, Y., Takahata, N., Nishio, Y., Fischer, T.P., Williams, S.N., 2001. Volcanic flux of nitrogen from the Earth. Chem. Geol. 171, 263–271. https://doi.org/10.1016/S0009-2541(00)00252-7

Sano, Y., Tokutake, T., Takahata, N., 2008. Accurate Measurement of Atmospheric Helium Isotopes. Anal. Sci. 24, 521–525. https://doi.org/10.2116/analsci.24.521

Scopelliti, G., Bellanca, A., Neri, R., 2011. Petrography and carbonate isotope stratigraphy from MIS AND-1B core, Antarctica: Evidence of the early Pliocene warming event. Glob. Planet. Change 76, 22–32. https://doi.org/10.1016/j.gloplacha.2010.11.006

Sims, K.W.W., Blichert-Toft, J., Kyle, P.R., Pichat, S., Gauthier, P.-J., Blusztajn, J., Kelly, P., Ball, L., Layne, G., 2008. A Sr, Nd, Hf, and Pb isotope perspective on the genesis and long-term evolution of alkaline magmas from Erebus volcano, Antarctica. J. Volcanol. Geotherm. Res. 177, 606–618. https://doi.org/doi: DOI: 10.1016/j.jvolgeores.2007.08.006

Symonds, R.B., Gerlach, T.M., Reed, M.H., 2001. Magmatic gas scrubbing: implications for volcano monitoring. J. Volcanol. Geotherm. Res. 108, 303–341. https://doi.org/10.1016/S0377-0273(00)00292-4

Szaran, J., 1997. Achievement of carbon isotope equilibrium in the system HCO^{3-} (solution) - CO^{2} (gas). Chem. Geol. 142, 79–86. https://doi.org/10.1016/S0009-2541(97)00077-6

Tebo, B.M., Davis, R.E., Anitori, R.P., Connell, L.B., Schiffman, P., Staudigel, H., 2015. Microbial communities in dark oligotrophic volcanic ice cave ecosystems of Mt. Erebus, Antarctica. Front. Microbiol. 6. https://doi.org/10.3389/fmicb.2015.00179

Thorstenson, D.C., Weeks, E.P., Haas, H., Busenberg, E., Plummer, L.N., Peters, C.A., 1998. Chemistry of unsaturated zone gases sampled in open boreholes at the crest of Yucca Mountain, Nevada: Data and basic concepts of chemical and physical processes in the mountain. Water Resour. Res. 34, 1507–1529. https://doi.org/10.1029/98WR00267

van Wyk de Vries, M., Bingham, R.G., Hein, A.S., 2018. A new volcanic province: an inventory of subglacial volcanoes in West Antarctica. Geol. Soc. Lond. Spec. Publ. 461, 231–248. https://doi.org/10.1144/SP461.7

Wardell, L.J., Kyle, P.R., Campbell, A.R., 2003. Carbon dioxide emissions from fumarolic ice towers, Mount Erebus volcano, Antarctica, in: Volcanic Degassing, Special Publication. Geological Society, London, pp. 231–246.

Woodcock, A.H., 1987. Mountain breathing revisited - the hyperventilation of a volcano cinder cone. Bull. Am. Meteorol. Soc. 68, 125–130. https://doi.org/10.1175/1520-0477(1987)068<0125:MBRHOA>2.0.CO;2

Zandomeneghi, D., Aster, R., Kyle, P.R., Barclay, A., Chaput, J., Knox, H., 2013. Internal structure of Erebus volcano, Antarctica imaged by high-resolution active-source seismic tomography and coda interferometry. J. Geophys. Res. Solid Earth 118, 1067–1078. https://doi.org/10.1002/jgrb.50073

Zhang, J., Quay, P.D., Wilbur, D.O., 1995. Carbon isotope fractionation during gas-water exchange and dissolution of CO2. Geochim. Cosmochim. Acta 59, 107–114.

Zimbelman, D.R., Rye, R.O., Landis, G.P., 2000. Fumaroles in ice caves on the summit of Mount Rainier: preliminar stable isotope, gas, and geochemical studies. J. Volcanol. Geotherm. Res. 97, 457–473. https://doi.org/10.1016/S0377-0273(99)00180-8

SM1: CO_2/O_2 ratios

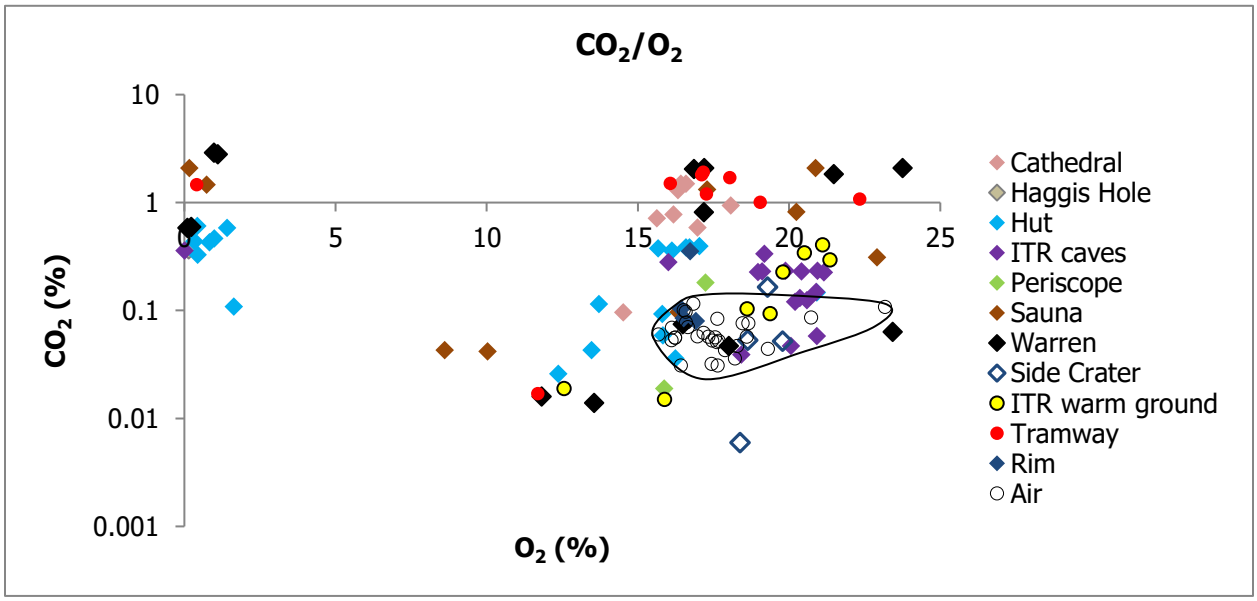

CO_2/O_2 from GC-QMS showing samples with air-like or higher CO_2 can be oxygen depleted. Samples with intermediate oxygen levels between air and oxygen depleted samples have CO_2 content of 140 - 1100 ppm (the most CO_2 depleted sample is from a Giggenbach bottle in 2015 that has airlike O_2 but about 60 ppm CO_2).

SM2: Table of samples analysed by GC-QMS with approximate latitude & longitude